NTNU

BACHELOR THESIS

The Effect of Radiation on Optical Elements for a Hyperspectral CubeSat Payload

Author:
Vebjørn Rogne Kristvik

Supervisor:
Kjersti Kleveland
Roger Birkeland

PROJECT CODE: IMA-B-13-2019
GRADING: PUBLIC

A thesis submitted in fulfilment of the requirements for the degree of Material Technology

at the

Department of Materials Science and Engineering
Faculty of Natural Sciences

June 3, 2019

NTNU
Norwegian University of Science and Technology

Dedicated to Ellen and Ivar

Abstract

NTNU SmallSat Lab seeks to build a low-cost & high-performance hyperspectral camera for detecting algae and plankton signatures from space. The camera is made from optical COTS components. It is, however, well known in the aerospace community that lenses exposed to radiation in space will brown over time. Radiation-induced optical degradation for all non-electrical components of the HyperSpectral Imager was studied in regard to space radiation conditions. Special emphasis was made on the objectives as it is a key optical component. After exposing the objective to 140 Gy with gamma radiation and performing optical characterisations optical degradation of 0.1% of the transitivity per Gy is observed. This degradation is due to a family of vacancies called colour centres, this makes the glass more absorbent to lower wavelengths of visible light. The camera will, therefore, be less reliable to detect the ocean signatures in the blue spectre, compared to the red. The optical testing techniques where largely successfully to both describe the optical changes in the components and are recommended for similar projects.

Sammendrag

NTNU SmallSat Lab har som mål å bygge en billig og hy ytelse hyperspectral-kamera for oppdage alge og plankton signaturer fra rommet. Kameraet er laget av optiske COTS komponenter. Det er imidlertid velkjent innen romfart industrien at linser som er utsatt for stråling i rommet, vil brune over tid. Arbeidet i denne rapporten studerer romstrålingsmiljøet og anvender det p optisk degradering for all ikke-elektriske komponenter i det hyperspektrale-kameraet. Det ble lagt hyere vekt p objektivet, som er en sentral komponent i transmisjonen av lys gjennom kameraet. Etter eksponering av objektivet til 140 Grey med gammastrling og utfrelse av optiske karakteriseringer, observeres optisk nedbrytning av 0,1% av transitiviteten for hver Grey ioniserende strling. Denne nedbrytningen er en del av klasse vakanser som kalles fargesentre, som gjr glasset mer absorberende for lave blgelengder av synlig lys. Kameraet vil derfor vre mindre plitelig for oppdage plankton signaturer i det blå spekteret, sammenlignet med det røde. De optiske testteknikkene var i stor grad vellykket til beskrive de optiske endringene i komponentene og anbefales for lignende prosjekter.

Preface

This report is written to fulfil my graduation requirements for a bachelor degree in material technology at NTNU (the Norwegian University of Science and Technology). This report is written and researched from January to June 2019. Project number for the bachelor is IMA-B-13-2019.

The project was undertaken for NTNU SmallSat Lab, a new organisation at NTNU dedicated to producing satellites.

My research question was formulated together with the NTNU SmallSat Lab manager, Evelyn Honoré-Livermore. The research was difficult, but conducting extensive investigation has allowed answering the question that we identified. Fortunately, I have had great support from supervisors and students at this projects.

I would like to thank my supervisors Kjersti Kleveland and Roger Birkeland for their excellent guidance and support during this process. Thank Andrey Kosinskiy for assistance in material testing. All my colleagues at NTNU SmallSat Lab have been of great support and motivation. A special thanks goes to Marie Henriksen for great support with optical characterisation at the radiation lab. Working close with Henrik Galtung, Tuan Tran and Tord Hansen Kaasa has been very productive and inspiring. DTU Risø was accompanying and helpful for testing radiation.

I hope you enjoy your reading.
Vebjørn Rogne Kristvik
Trondheim, June 3rd 2019

Table of Contents

Abbreviations

AMOS	Centre for Autonomous Marine Operations and Systems
COTS	Commersial off the shelf
EDS	Energy-Dispersive Spectroscopy
ECSS	European Cooperation for Space Standardization
HSI	Hyper Spectral Imager
HYPSO	HYper-spectral Smallsat for Ocean observation
LEO	Low Earth Orbit
NTNU	Norwegian University of Science and Technology
UV	Ultraviolet
VUV	Vacuum Ultraviolet
PKA	Primary Knock-on Atom
SKA	Secondary Knock-on Atom
SEM	Scanning Electron Microscopy
STK	Systems Tool Kit
XRD	X-ray Diffraction

Chapter 1

Introduction

1.1 The HYPSO Mission

The HYPSO (HYper-spectral Smallsat for Ocean observation) mission is intended to be a science-oriented satellite, to study marine life remotely from space through observing ocean colour. The satellite bus is built by NanoAvionics, by design and specification of NTNU SmallSat Lab. SmallSat Lab is the developer of the satellite's payloads, where the hyperspectral imager (HSI) is the main payload, and the focus of this report. In Figure 1.1 is the HYPSO logo, illustrating the satellite observing ocean colour [1].

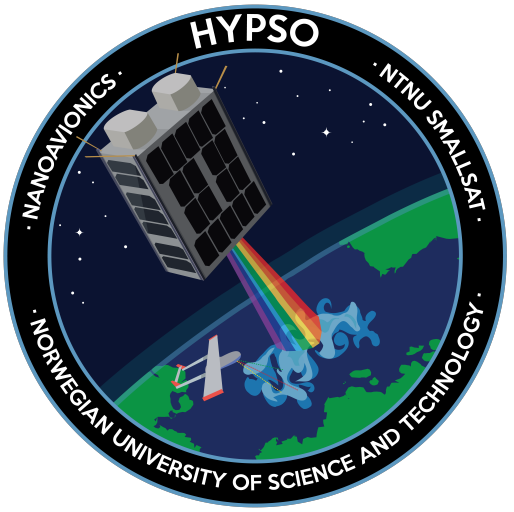

Figure 1.1: The HYPSO logo, featuring the satellite and unmanned areal vehicle observing ocean colour with hyperspectral imaging [1].

The hyperspectral camera takes photographs while registering around a hundred different wavelengths in the visible and infrared spectrum. To recognise colour signatures of plankton and algae colonies in coastal waters. Oceanographers can use these data to study the effects of climate change and human impact on the ocean [2]. The HYPSO satellite is to work together in a concert of autonomous vehicles such aerial, surface and underwater drones, shown in Figure 1.2. These autonomous vehicles will work together to monitor marine life from different altitudes, and with different payloads. This is the goal of NTNU AMOS (Centre for Autonomous Marine Operations and Systems), in which the HYPSO satellite is one actor [3].

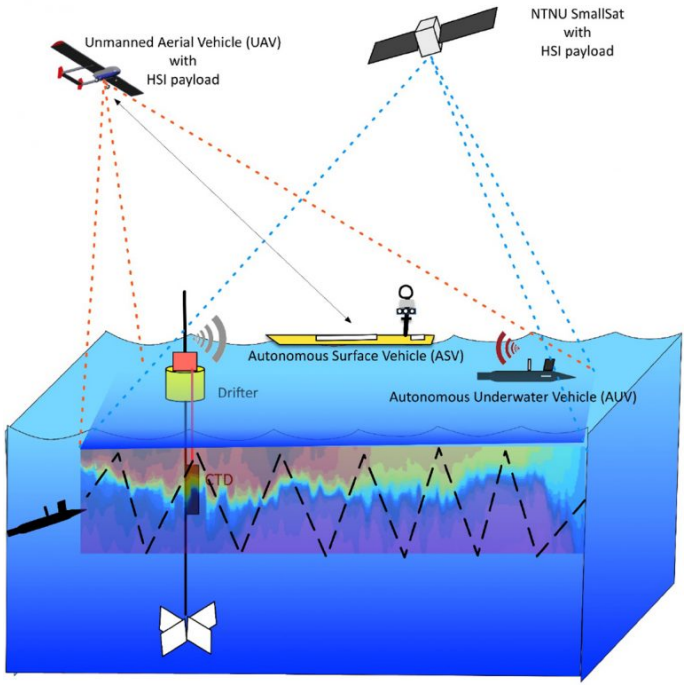

Figure 1.2: The grander plan of AMOS is to have a constellation of autonomous vehicles surveying and monitoring the ocean [1].

The HYPSO satellite is made at the SmallSat Lab at NTNU and is the first satellite project from this organisation. Here a multidisciplinary team of bachelor, master, PhDs and Post.Docs, from a wide range of departments across NTNU work together to build satellites [1]. The HYPSO project is sponsored by the Research Council of Norway, in association with NTNU and Norwegian Space Agency. With the goal of enabling low-cost & high-performance hyperspectral imaging on a satellite. The satellite is being designed as a CubeSat, built of COTS (Commercial Off The-Shelf) components. The satellite will orbit Earth at a polar orbit of 500 km above ground, crossing Norwegian waters 8 to 10 times a week [3]. Launch date is set for Q4 2020, and full success criteria is 5 years of fully functional hyperspectral data acquisition. After about 8 years, the satellite will deorbit due to drag, and burn up safely in the atmosphere [2].

A CubeSat is a small satellite that follows the CubeSat standard set by California Polytechnic State University and Stanford university in 1999 [4]. The CubeSat standard constrains geometry and materials, but is ideal for rapid production. By choosing COTS components over space-graded components this project can cut development and deployment costs and time , but the satellite project itself has to evaluate space robustness of any non-space graded components [5, 6].

1.2 Reliability and Mission Requirements

Although a CubeSat is manageable to design and finance, the fact is that until now, they have been unreliable and most fail to achieve their full mission objective. Figure 1.3 shows how few missions reach their full mission criteria and how many satellites are dead upon arrival in space, or lost prematurely [7]. The main reason for all these failures are the highly challenging phases a CubeSat will face in its life time [8]. From launch with extreme forces and shaking, to the space environment with high temperature changes, micro-meteorites and vacuum to name a few [5]. Radiation is one of these environmental concerns and is due to the bombardment of high energy particles and electromagnetic radiation. However, radiation effects are for the most part accumulated over the spacecrafts lifetime and is unlikely to cause an early loss.

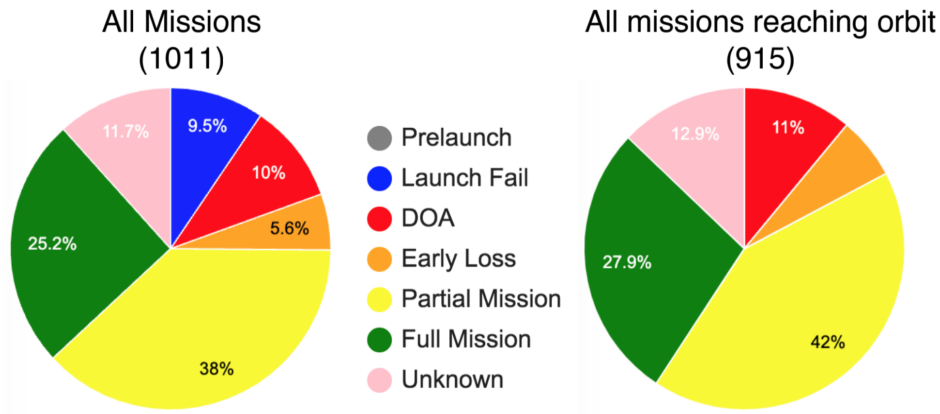

Figure 1.3: Mission reliability for CubeSats since 2000[7].

The HYPSO satellite is designed to have a lifetime of five years with full success of algae and plankton imaging [9]. To quantify this, the mission has defined several missions and scientific requirements. Presented in Table 1.1 are relevant scientific requirements for the optical payloads. Measuring the amount of these organic molekules and detecting when these algea bloom are of interest among oceanographers. are the Radiation could reduce or hinder the camera in detecting of measuring these signals [10].

Table 1.1: The oceanographers requires the payload to be able to measure and identify these organic molecule and algae concentrations [9]

Scientific requirements	**Wavelength [nm]**
Should measure Particulate inorganic carbon	443, 555, 670, 765, 865
Should measure Particulate organic carbon	443, 490, 555
Should measure fluorescence line height	557, 678, 710, 748
Should measure dissolved organic matter/carbon	350-555
Should detect Chlorophyll-b	655
Should detect Carotenoids	470
Should detect Phycoerythrin	490, 550
Should detect Phycocyanin	620

The HYPSO mechanical team (author included) has during the period of this report worked with multiple environmental issues for the payload. Parties interested in the reliability and mechanical design of this satellite can read *Implementation of FMECA in Small Satellite Development* freely available from NTNU.

1.3 Problem Statement

It is well known in the aerospace community that lenses exposed to radiation in space will brown over time. This makes radiation an issue for the project mission goal.

In response to this problem, this study will investigate and evaluate the effect of radiation to the non-electric camera components. the lenses and light controlling components of the instrument, over mission lifetime. The work performed will cover: Theoretical study of the space environment, including a simulation of the expected orbit in order to determine the ammount of radiation the satellite will be exposed to. Then, the actual optical components used in the HSI will be exposed to radiation in an experiment, followed by optical characterisation of the irradiated sample and a control sample. Further, material analysis of the optical components will be performed. The effects of radiation on glasses will be studied and tested with gamma radiation. And a method for characterizing these must be planned

Chapter 2

Theory

The purpose of this chapter is to inform the reader of the necessary details concerning the hyper-spectral camera, optical properties, space radiation environment and the radiation effects on key materials.

2.1 The Hyper-Spectral Payload

Hyper spectral imaging is a method of producing images while capturing over a hundred different wavelengths. A hyper spectral image is therefore regarded as a three-dimensional image, that can detect optical signatures [11]. Figure 2.1 illustrates this by comparing a hyper-spectral image to a regular red, green and blue image.Typically, a hyperspectral camera is defined as capable of producing an image with more than 30 spectral bands, it is however not uncommon with 100 spectral bands or more [12].

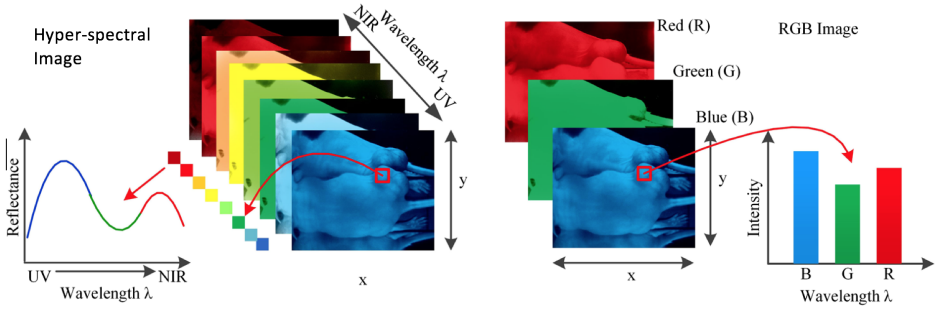

Figure 2.1: Comparison between a hyper-spectral and regular red, green and blue image. Hyper-spectral images are three-dimensional dataset of a two-dimensional image on each wavelength [11].

Figure 2.2 visualises the optical components in hyperspectral camera. The camera is just observing a single line through a slit which then become diffracted to by a grating.

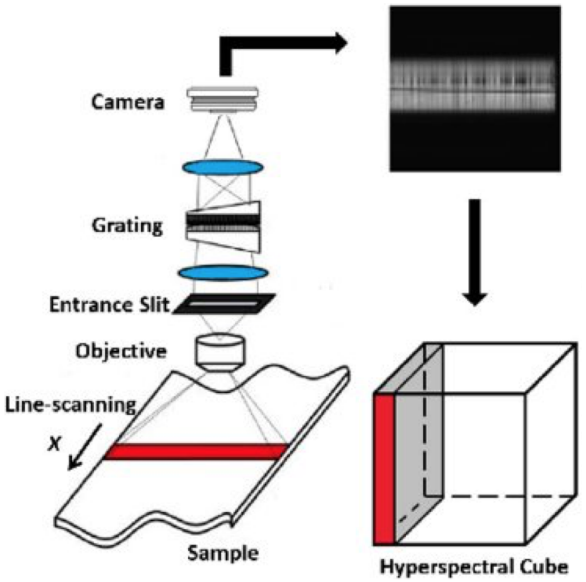

Figure 2.2: The principal of Hyper-spectral imaging is to scan the light of a single line and split this light into fractions. The three dimensional image is called a hyperspectral cube, and is assembled from multiple line scanning [13]

2.1.1 HyperSpectral Imager (HSI) Components

The camera, referred to as the HSI is made up of several optical Commercial Off-The-Shelf (COTS) components from various laboratory and photography and producers. The camera registers wavelengths from 400 to 800 nm, which means it covers the whole spectrum of visible light and a small portion of infrared [14].

There where one built at the start of this bachelor project, and two more where built at the end. This meant that the HSI could not be changed, to test irradiated parts within the design. Figure 2.3 displaces the HSI and its primecomponentss of interest in this report. The camera sensor is also referred to, as it is used within testing to characterise transmission loss through the objective.

2.1.2 Objective

The component referred to as the objective is a 50 mm adjustable lens for visible and near infrared light made by Edmund Optics [16]. It is called a objective to not confuse the reader when discussing the individual lenses inside. In the space the focus shall be fixed at infinity (no final focal point) [14, 15].

Edmund optics lack any descriptive datasheets for glass series/material, or this unit is made. The impact of radiation in this unit is primarily reduces transmittance due to radiation induced colour in the lenses. It is possible that radiation can change the polarity and thereby impact diffraction, and shift the focus. However, this is out of scope for this

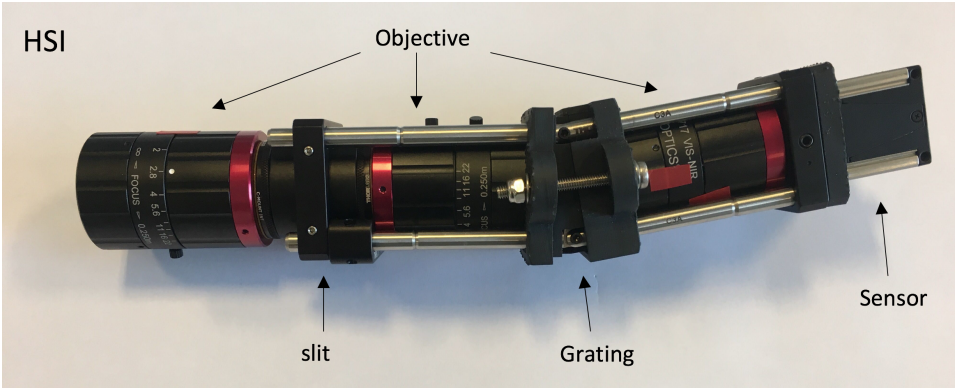

Figure 2.3: HSI design as spring 2019 [15].

report.

2.1.3 Grating

The grating decomposes white light into components of varying wavelengths as a prism of multiple blazed groves [17]. Figure 2.4a is a image of the grating, showing diffracted light in a rainbow pattern. Figure 2.4b illustrates the prismatic groves that diffract the light.

The glass substrate is Schott B270 [17], which is particular series of silicon dioxide glass [18]. The impact of radiation in this unit is primarily reduction of transmittance due to radiation induced vacancies in the glass. A change in diffraction index due to change in polarity can not be ruled out, but is outside of scope.

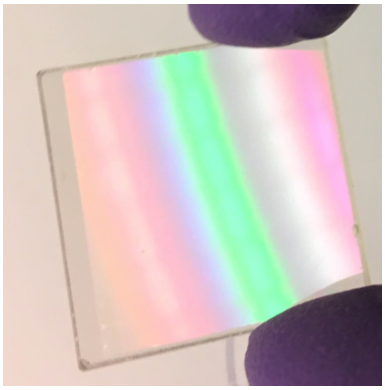

(a) Picture of the grating

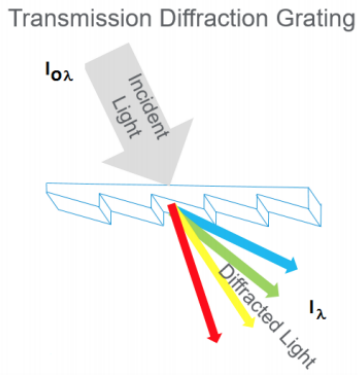

(b) Visual description of how light is diffracted through a grating [19].

Figure 2.4: Picture and illustration of the grating

2.1.4 Slit

The slit is a disk with a precision cut 50 μm width line, for letting light through as a single line. There are actually two candidates for the slit, one provided by Thorlabs and one provided by Ealing optics. Their function is the same, but they differ in materials. The Thorlabs slit is cut on a black oxide coated stainless steel disk, supported by a aluminium frame [20]. While the Ealing s is cut on a chromium coated glass disk [21]. The Thorlabs slit is the one in use in all the current built HSIs [14].

(a) The Thorlabs slit is made as a cut thought a black oxide stainless steel disk [20].

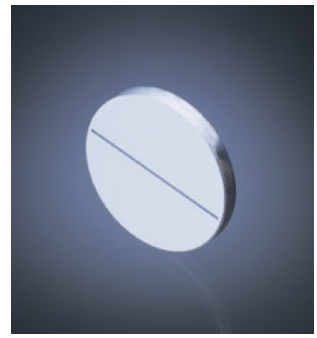

(b) The Ealing slit is made as a cut throught a chromium coated glass substrate [21].

Figure 2.5: Thorlabs and Ealing slit

The material composition in the slit is brought up because of a mechanism with protons and metals that produces hydrogen gas underneath metallic surfaces[22]. This is covered in Section 2.5.1, but only briefly as it is outside the problem statement.

2.1.5 Aluminium Support Structure

The HSI camera is supported by an aluminium structure to mitigate shock, vibration and thermal effects on the camera. It was never designed as radiation shielding it will absorb energy, preventing it from penetrating into the camera parts. The geometry of the aluminium structure is complex and will offer more radiation protection in its base structure of 7 mm than the less shielded top. The brackets holding the objective in place is 3 mm thick and covering much of objective, but not entirely. The grating is the most shielded part with shielding of 6 mm in every direction [23].

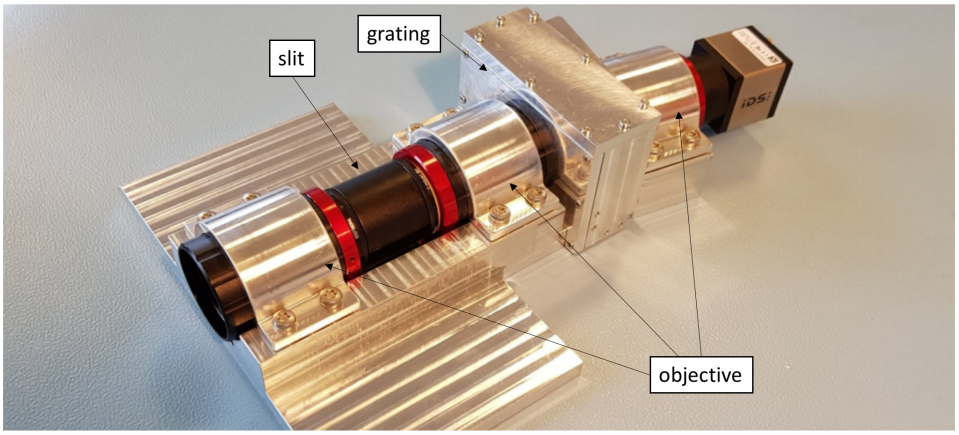

Figure 2.6: HSI in its aluminium support structure, placement of optical parts are underneath [23].

2.2 Visible light

This assignment focuses primarily on radiation effects on optical material properties. Photons can be both ionising or non-ionising dependent on how much energy is contained within the photon. Visible light consists of photons with a wavelength between 400 and 700 nm. Wavelengths shorter than 400 nm are ultraviolet (UV), X-rays and gamma rays, these photons are energetic enough to ionise electrons from the nucleus of an atom. Hence they are regarded as ionising radiation [24, 25].

All photons are electromagnetic radiation, however a distinction is expressed in this report to refer to the observable photons for the HSI as ”visible light”. This distinction is made to avoid confusion, as electromagnetic radiation is both used for exposing samples to radiation, and as a test medium to characterise optical properties. Section 2.3.1 will cover ionising electromagnetic radiation.

When light proceeds from one medium into another (e.g., from gas into a solid substance), it can get transmitted, absorbed or reflected in the interaction between the two media. This is given by equation 2.1, the intensity of the photon must be equal to the sum of transmitted, absorbed and reflected intensity, denoted as I_T, I_a and I_R respectively [26].

$$I_0 = I_T + I_a + I_R \tag{2.1}$$

2.3 Absorption of Ionising Radiation

Radiation is defined as the emission of energy as electromagnetic waves or as moving subatomic particles, capable of ionising matter [22]. This energy can either be absorbed by electrons to excite/ionise itself, or to the nucleus to displace it to a new position. Elements can also absorb the entire particle and trigger a nuclear reaction, but this requires considerably higher energy then what is normal in LEO, and is therefore excluded from this thesis [27].

2.3.1 Radiation Types

The types of radiation differ in mass, charge, speed and consequently energy, and thus they dissipate energy differently. Larger particles dissipate faster than smaller particles, and are therefore considerably easier to shield [28]. Positively charged particles interact more with electrons, while negatively charged atoms interact with the electric field of the nucleus [29]. This means that different atoms are more suited to stopping different types of radiation. It is however, experimentally found that the resulting defects in materials are quite similar [30]. This is the same for glasses, where it is generally admitted that different types of radiation produce similar absorption effects [31]. However, there are some research hinting to displacement playing a larger role than ionisation [27].

Table 2.1 summarises the dominant absorption effect on SiO_2. Note that UV light is not energetic enought to ionzie SiO_2 [28].

Table 2.1: Ionising radiation types and their dominant absorption effect on SiO_2 [28].

Absorption	**Alpha**	**Proton**	**Electron**	**Neutron**	**UV**	**X-ray**	**gamma**
Ionising	x	x	x			x	x
Displacing				x			

Alpha Particles

The large size, weight, and charge of the alpha particles makes them the disperse energy to other atoms faster than any other radiation type. This is seen in Figure 2.7 where the projected range of alpha particles are compared to protons. One can see that a alpha particle reach a tenth of the distance of a equally energetic proton.

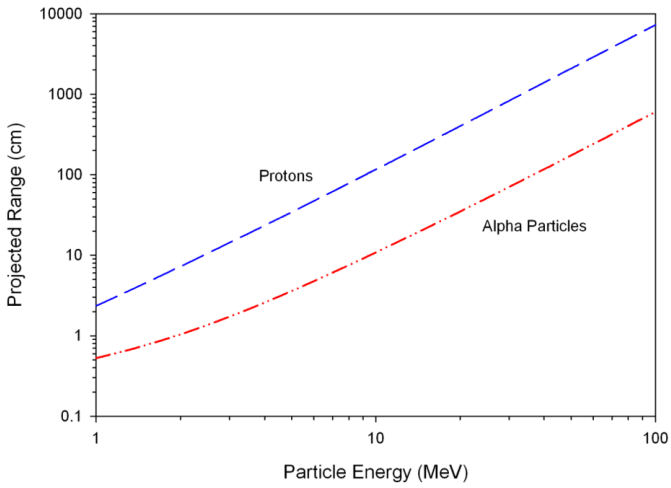

Figure 2.7: Projected range of alpha and protons in SiO_2 [32]

Alpha particles transfer most of their energy to electrons causing them to be either excited or ionised. The energy can also be transferred to the atom and thus displacing it, but alpha particles are considered predominantly ionising [29, 32].

Protons

Energetic protons behave quite similar to alpha particles as this also is a positively charged particle. However, the proton particles may traverse through much more matter before dispersing there energy [22]. This is seen in Figure 2.8 where radiation distribute increasing energy after the first 0.4 μm of SiO_2 with 30 keV [32].

Electrons

Electron radiation, also known as β radiation in nuclear physics, consists of high speed negative charged electrons as the name implies. Electrons dissipate their energy primarily to other electrons via excitation mechanics [33]. 1-10 MeV electrons will be entirely shielded by 10 mm aluminium [28].

Bremsstrahlung is an excitation mechanism where the electron is slowed down so rapidly that it creates secondary X-rays. Which absorption mechanism is most likely depending upon strength of electric field, with ionisation occruing in lighter element, and bremsstrahlung in heavier elements. It can therefore be favourable to slow a beta particle by using a lighter substance such as aluminium or plastic [28].

Neutrons

Neutron radiation is an uncharged particle that cause indirect ionisation by colliding with other atoms absorbing energy to reduce its speed. The energy is linked to speed, and neutrons are classed by their speed as thermal less than 1 eV, intermediate 1 eV between

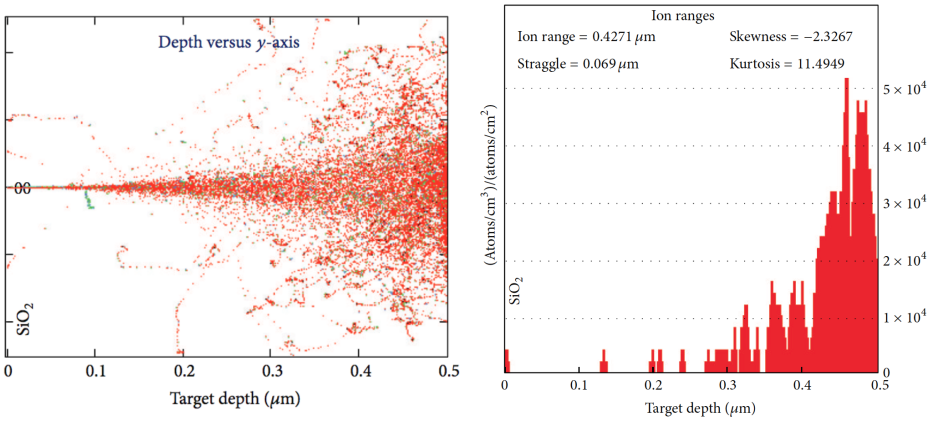

(a) Simulated trajectory of 50 keV protons passing through 0,5 μm layer of SiO_2.

(b) Distribution of stopped protons along the material .

Figure 2.8: Dept of protons in SiO_2 [32]

100 keV and fast neutrons above 100 keV. Whereas thermal neutrons interact elastic with the particle, while fast neutrons interact violently causing displacement and emitting secondary gamma or/and X-rays [28].

Since Neutron radiation is charge-less this radiation does not interact with the electromagnetic field of the atom, and thus neutrons can penetrate deep into matter. Neutrons have three main interaction mechanisms that can cause ionisation or emitting radioactive sources [34].

Elastic scatter: transfers the energy as momentum to the nucleus, like snooker balls. This requires interaction between a low energetic neutron, or a light element, or both. Materials with low atomic weight are therefore preferable to slow down neutrons.

Inelastic scatter: Similar to elastic scattering, but some of the energy excites the nucleus, which gets de-exited by emitting gamma or X-rays.

Ionising Electromagnetic Radiation

Ionising electromagnetic radiation are grouped as UV, X-ray and gamma-rays according to their energy and how they are formed [29]. UV light is the least energetic, and will not ionise SiO_2. X-rays carries energy in the range of 100 eV to 100 keV, with the higher energetic capable of ionising SiO_2 [27]. Gamma-rays carry energy in excess of 100 keV, and is highly ionising. Gamma rays can produce secondary electrons in the photoelectric effect that are energetic enough to displace atoms [27].

Ionising electromagnetic radiation are attenuated exponentially when passing through matter. The dose after thickness (t) can be written as equation 2.2. Where D_t is the dose rate at shielding thickness, D_0 is initial dose, is a material dependant absorption coefficient [m^-1]. It is difficult to absorb ionising electromagnetic radiation completely, and travels large distance even in dense media. [29].

$$D_t = D_0 exp^{-t} \tag{2.2}$$

The three most important interactions between high energy photons and matter are the *photoelectric effect, Compton scattering* and *par-production*. Which of these effect befall depends on the energy and the strength of the electric field [29].

Photoelectric effect: The energy of the photon is transferred to an electron, which is emitted with all the energy of the initial photon. The photon is in this case completely absorbed. This requires high initial energy to overcome the electrons bonding energy, however, gamma and some X-ray have more than sufficient energy for this [28, 29].

Compton scattering: is similar to the photoelectric effect, but only parts of the photons energy is transferred to the electron. Resulting in a scattered less energetic photon. Cobalt-60 irradiation causes damage chiefly through the secondary electrons produced through the Compton interaction [35**?**].

Pair-production: If a photon with energy above 1.022 MeV gets close enough to the nucleus and its intense electric field, the photon may be converted to an electron-positron ($e^- : e^+$) pair. Any excess energy is converted to momentum of ($e^- : e^+$) pair [35].

Cobalt-60 produces gamma rays by the nuclear transformation in equation 2.3. Where a stable ^{59}Co absorbs a neutron (η) and transforms to ^{60}Co. In its current form right after accepting the neutron it is both nuclear unstable, and having more energy then it should. ^{60}Co will then immediately relax itself by emitting energy as a gamma ray, but it is still nuclear unstable. With a half-life of 5.272 years ^{60}Co decays to Nickle-60 with beta decay. Once ^{60}Ni is formed it will relax itself by emitting two wavelengths of high-energy gamma-rays at 1.17 and 1.33 MeV (average 1.25 MeV). It is these two gamma rays one uses for radiation exposure testing [36, 37].

$$^{59}_{27}Co \xrightarrow[5cm]{\eta} ^{60}_{27}Co + \gamma \xrightarrow[5cm]{\beta^-} ^{60}_{28}Ni + \gamma(\sim 1.25MeV) \tag{2.3}$$

2.3.2 Ionisation

Ionising radiation is the removal of one or more electrons from the atom by incoming energy. Removing a electron might split molecules and can modify physical and chemical properties of the irradiated materials. The mechanism behind the ionisation is the same as with an excitation, except the energy is high enough to remove the electron completely [38]. Figure 2.9 illustrates this with a electron ejected from its orbit by incoming energy.

The SI unit for absorbed ionised energy is the Grey (Gy) and is equal to joules of ionised particles per kilogram matter. It is however common to see the Rad used instead of Gy. This is an alternative unit for ionised energy that predates the Gy, 100 Rad equals 1 Gy [28].

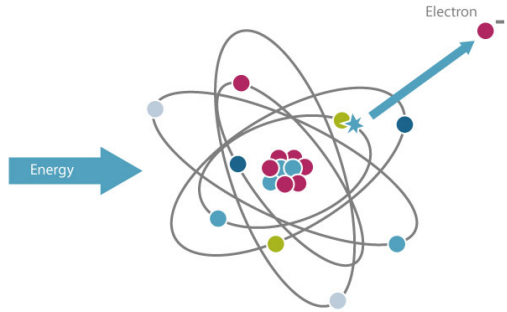

Figure 2.9: Energy exciting a electron beyond the every electron orbit [39].

2.3.3 Atomic Displacement

The kinetic energy of small particles can transfer momentum directly to an atom to displace this atom to a new position. If the recoiled atom is energetic enough it can displace secondary atoms as a cascade of vacancies. Figure 2.10 illustrates the relationship between energy of the incoming particle, recoil energy and number of cascades. The primary knock-on atom (PKA) can only be displaced if the transferred energy is higher than a threshold energy T_d of the material. T_d in silicon is in the order of 25 eV, and $\sim$ 5keV for producing a cluster [40, 35]. The maximum kinetic energy transferred from electron radiation to a nucleus is given by equation 2.4.

$$T_{max} = \frac{2(E + 2mc^2)E}{(Mc^2} \tag{2.4}$$

Where E and m is the energy and mass of the incoming particle, M is the mass of the nucleus and c is the light constant. Electromagnetic radiation cannot directly displace atoms, but high energy photons can generate secondary electrons thought the photoelectric effect, that can produce displacement. For Gamma rays from cobalt-60 these secondary electrons have a energy of around 1 MeV. A 1 MeV electron will transfer a maximum of 155 eV to a silicon atom. This produces vacancies in the PKA, but is not enough energy to generate a cascade [35]. Larger particles (e.g. neutrons and protons) with energy less than 100 MeV, transfer energy through elastic scattering. It is therefore more appropriate to use equation 2.5 from classical mechanics to calculate T_{max}.

$$T_{max} = \frac{4mM}{(m + M)^2} \tag{2.5}$$

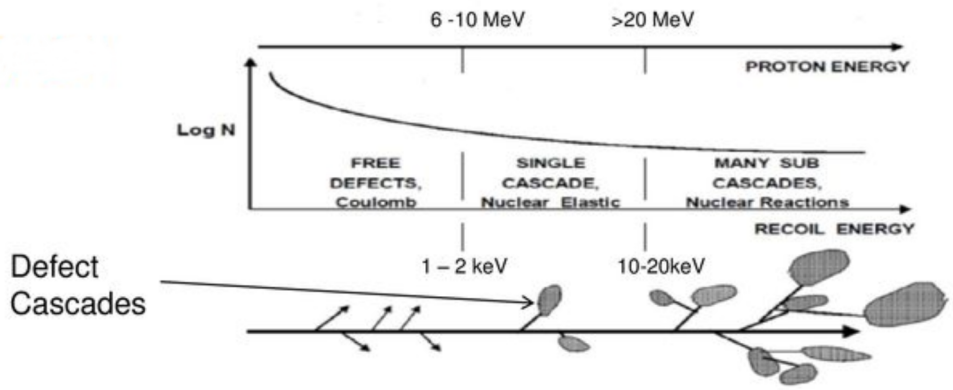

Figure 2.10: Relationship between energy of incoming particle and cascade severity, with a proton in silicon as example. It requires more than 6-10 MeV in the incoming proton to knock the secondary atom hard enough to produce a cascade [41].

Generally, only a smaller fraction of the particle energy goes into displacement, most goes into ionisation. The transferred energy in the collision may dissipate thermally. Not all vacancies become stable, in fact most recombine by themselves, either immediately or when enough heat is applied for recombinations to occur by diffusion [41].

2.4 Space Radiation Environment

The space radiation environment consists of particles and ionising electromagnetic radiation ejected from our sun or other celestial entities outside our solar system. Ionising electromagnetic radiation is also striking spacecraft in this environment, but the space environment is dominated by particles [42]. The sun ejects particles constantly as solar wind, but also, sporadically as solar flares or even more rare, but more destructive coronal mass ejection [43, 44].

Earth's magnetic field shields the surface and the lower orbits from most of the radiation, by diverting and trapping particles along the magnetic field lines, thus, making these sources very effective in polar regions (above $\sim 60^\circ$ inclination), and introduces a third radiation source: trapped radiation in earth' magnetic field. This source consists of an internal and radiation belt made of protons and electrons, and an external of electrons [34]. The trapped touches LEO (Low Earth Orbit) in the polar regions and in areas of weak magnetic field strength [45].

When considering the space radiation environment for a spacecraft it is important to have the orbit of the spacecraft in mind as that will determine which source dominates and the amount of radiation. The HYPSO satellite will orbit the Earth every 90 minute in a sun-synchronous orbit with an altitude of 500 km above ground and inclination of 97° [2]. Sun-synchronous means the orbit follows the Earths spin from the suns perspective. Inclination is the degree of tilt from the equator, thus 97° is 7° off the North and South pole [5]. This essentially means that the satellite will enter the South Atlantic anomaly once every day, and each polar region every 45 minutes. Figure 2.11 is the orbit visualised in a top view. From this view, the orbit appears as a curve over the poles, when it is a straight line on a curved surface.

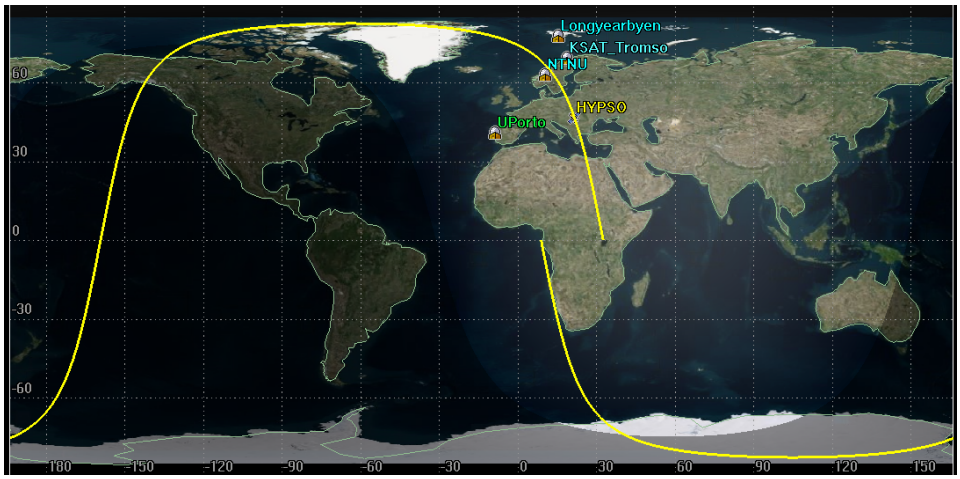

Figure 2.11: One orbit 90-minute orbit [2].

2.4.1 Solar Radiation

Solar wind is a constant flux of protons (95%) and α particles speed 300 - 900 km/s, and ionising electromagnetic radiation up to low intensity X-ray [46]. These particles are of low energy and will in most cases be diverted by the geomagnetic field or become trapped, the particles that hits spacecraft have little impact and will be stopped by very little shielding [47].

Solar flares are bright and energetic bursts from the suns surface. Releasing mostly electrons, but also energetic protons (up to 500 MeV), and heavy-ions (up to 10 MeV per nucleon) along with electromagnetic radiation in every wavelength [47, 32]. Solar flares are directional and random occurring events, but associated with solar activity, hence difficult to predict, but more likely during high solar activity. Solar activity follows a eleven-year cycle, with a seven-year period of high solar activity and quiescent four-year period [34]. This can be seen in Figure 2.12, and is measured by counting sunspots (black spots) on the suns surface. Sunspots are linked to the formation of solar flares and coronal mass ejections, and a high number of sunspots indicate a higher likelihood of solar flares and / coronal mass ejection [48].

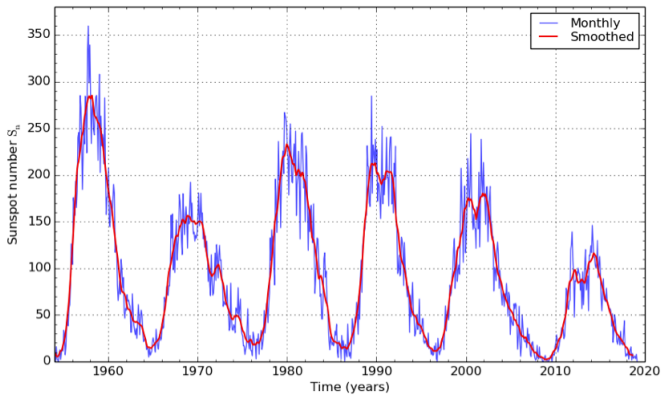

Figure 2.12: Monthly and smoothed sunspot number by the Royal Observatory of Belgium [49].

Coronal mass ejections are larger explosions that happen less frequently than solar flares, but also follow the solar cycle. These outburst spill out electromagnetic radiation (X and γ-rays) as well as, energetic electrons, heavy-ions (up to uranium) and α particles, flowing with speed a of 50 - 2500 km/s. These high-energy particles have largest effect on spacecrafts, as they carry enough energy to reach spacecraft protected by the Earth magnetic field, and penetrate thick layers of radiation shielding [47, 50].

Neutrons ejected by the sun decay rapidly before reaching the Earth, making it only considered a radiation source for missions close to the sun [51].

2.4.2 Trapped Radiation

Earth's radiation belts are also referred to as the Van Allen belts. Particles are trapped in a torus (doughnut like) shape surrounding Earth's equator. For the most part, these belts behave as two separate belts [52]. The inner belt consists of an energetic proton belt (up to 600 MeV) and an energetic electrons belt (1-10 MeV) [47]. In Figure 2.13 one can see the inner belt illustrated on both sides of Earth, as it consists of both protons and electrons. The outer Van Allen belt consists predominantly of energetic electrons (10-100 MeV), and is seen right of Earth in Figure 2.13. Proton and electron densities are highest at 0° inclination, whilst the electrons reach much closer to earth at the polar caps [34].

The south Atlantic Ocean has weaker magnetic field strength than the rest of the planet, making the internal radiation belt dip to 200 km over this location [45].

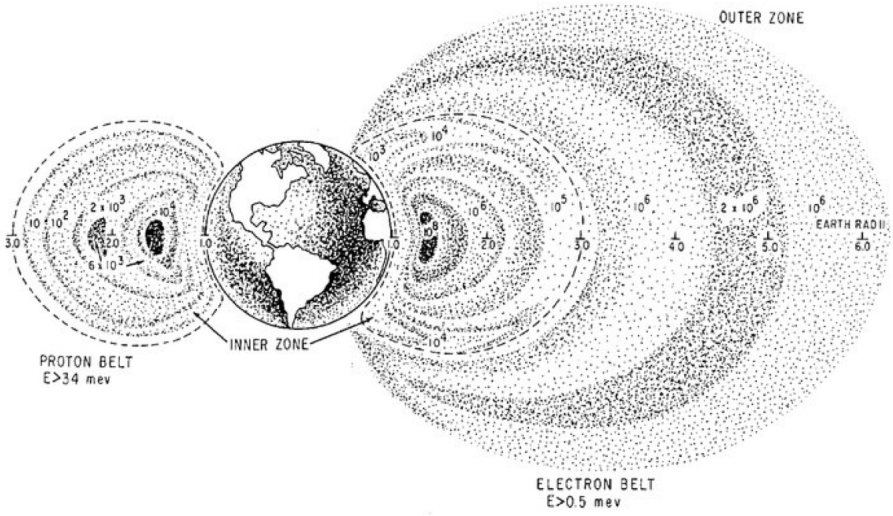

Figure 2.13: Trapped protons are only found in the inner belt, trapped electrons are found in both belts, with higher concentrations in the outer belt [53].

2.4.3 Cosmic Radiation

Galactic cosmic rays is a radiation source from outside our solar system, generated from supernovae and other violent events from the distant Universe. These rays constitute of an isotropic field of particles which comprises of about 85% protons, 14% α particles and 1% heavy ions at energies in the range 10 MeV to tens of GeV per nucleon.

Earth is protected from GCR by both the magnetic field of our own planet and of the sun. The suns magnetic field weakens during high solar activity, thus making the strength of galactic cosmic rays anti-correlative with the solar cycle [47].

Cosmic rays are primarily an issue for electronic equipment and humans, according to the ECSS-E-10-04C space environment [51]. This is evident in Figure 2.14 where one can see that cosmic rays produce single events effects in electronic equipment.

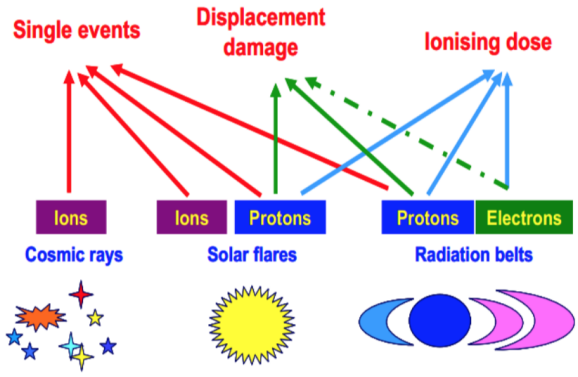

Figure 2.14: A simplified illustration of the space environment sources, there radiation products and there following radiation mechanism. [47].

2.4.4 Simulation of the Radiation Environment

The space radiation environment can be simulated based on orbital parameters. It is possible to estimate: radiation flux along orbit, shielding thickness penetration and Total ionised Dose. This is based on models for Earth's magnetic field, Earth's radiation belts, solar particles and cosmic radiation. However there are currently no models for alpha particles or direct electromagnetic radiation, but secondary electromagnetic radiation from bremsstrahlung can be modelled [54, 55, 56].

The simulation is performed as a numerical analysis at a given point in space, or several points in an orbit. In addition to choosing the number of points per orbit, one also has to set the number of orbits to calculated [57]. An increased number of points per orbit and orbits increases the quality of the simulation, but at the cost of increased simulation time. As with any simulation tool this is values to controlled by a convergence study. A convergence study is performed by gradually increasing the value until the result converges towards a fixed value [58].

Figure 2.15 is one of the radiation simulations that where conducted with Systems Tool Kit (STK), prior to this author getting involved in this project. STK is dedicated tool to study space missions, and simulate a wide viraity of aerospace problems [59]. This simulation shows accumulated dose over a year for three different thicknesses of aluminium shielding [2]. The units are the rad and Mils, which are a thousand of an inch [60]. Table 2.2 presents the values in imperial and Si units, and account for true orbit duration.

Table 2.2: Summary of simulation, displayed in imperial and SI units.

Sheilding		1 year orbit duration		5 years orbit duration	
Mils	mm	rad	Gy	rad	Gy
82.5	2.09	239	2.39	1195	12.0
232	5.88	165	1.65	825	8.25
478	11.6	127	1.27	635	6.35

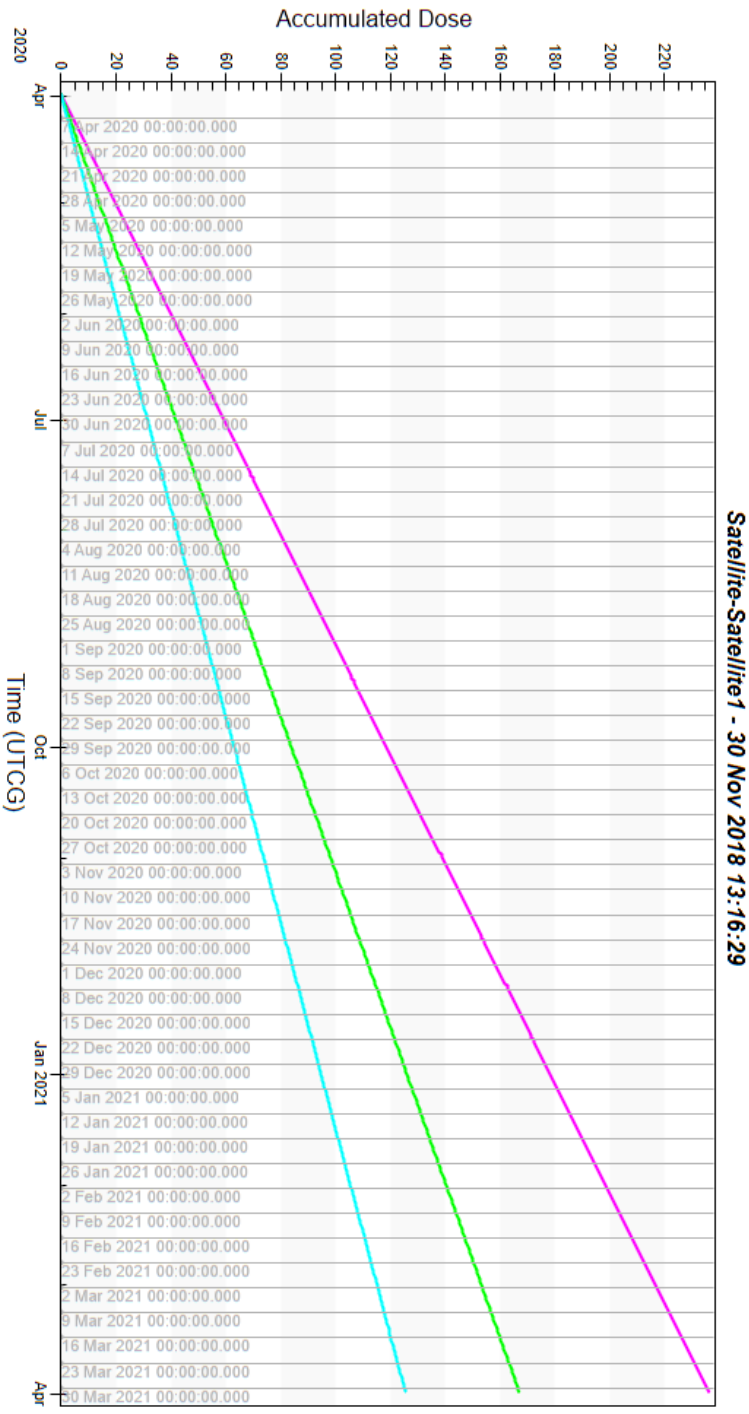

Figure 2.15: STK sheilding penetration analysis in 82.5 Mils (2.09 mm), 233 Mils (5.88 mm) and 478 Mils (11.6 mm) aluminium .

2.5 Radiation Effects on Material Classes and Glass

This section performs a general introduction to radiation on metals, polymers and ceramics, and a detailed description of radiation on glasses.

2.5.1 Radiation on Metals and Alloys

Metals and alloys have a large number of non-localised electrons. These free electrons make metals more robust towards ionisation as there is always an abundance of electrons. Displacement is consequential as it deforms the crystal lattice and introduces point defects. The consequence for the subjected metal is reduced ductility, increased hardness and embitterment. Radiation effect also make the material more susceptible to environmental induced degradation, such as stress crack corrosion [61, 26].

Proton radiation can recombine with non-localised electrons in the metal, to form hydrogen under the metal surface. This is seen in Figure 2.16 of proton irradiated aluminium. Hydrogen formation can create hydrogen bubbles under the metal surface and induce hydrogen embitterment. [22]. Hydrogen bubbles could cause a metallic surface treatment to flake . This would be highly destructive for the slit function in the HSI.

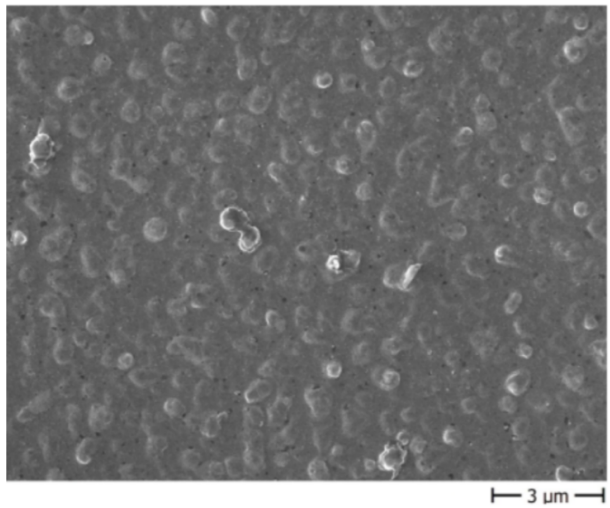

Figure 2.16: SEM image of aluminium irradiated with 2.5 keV protons [22].

Space design metals and their mechanical properties perform a key role in launch, where shock and vibrations are extremely high. Metallic support structures are engineered to handle these stresses and are generally over engineered when free floating in space. Thus, embitterment and reduced ductility is not normally considered an issue in space mechanical design [6, 54].

2.5.2 Radiation Effects in Polymers

Polymers are highly susceptible to radiation as can be seen with everyday plastics that get degraded by UV light to lose colour and become brittle [62]. Physical and mechanical properties can significantly change due to small amounts of radiation, with the extent of these changes are dependent upon the chemical structure of a polymer. The radiation induced chemical reactions result in increased chain crosslinking or its opposite chain scissioning. Where crosslinking increases molecular weight by forming larger polymer chains. Chain scissioning cuts off parts of the original polymer chain and reduces molecular weight. These two processes will primarily determine changes in physical and mechanical properties but radiation on polymers can also realise outgassable material on otherwise non-outgassable polymers. Outgassing is another material degradation of high importance in space, but outside of scope for this thesis [63, 64].

2.5.3 Radiation Effects in Ceramics

Ceramics present a diverse class of solids with structures varying from simple to complex, and bonding can be all from highly ionic to covalent, and in some cases partially metallic. Band gaps of ceramics can be everything from wide-gap insulators to superconductors, and glasses. Radiation effects on this material class is far more complex than metals and polymers. The primary radiation effect for the general material group are atomic displacement, which subsequently forms Frenkle pairs (displaced ion) [65].

Radiation increases amorphization and can significantly alter electrical and thermal conductivity. The density of the ceramic is also prone to decrease, as open pores get converted to closed pores [66].

2.5.4 Radiation Effects on Optical Properties for Silica Glass

Radiation science on optical properties and defects on crystalline and amorphous SiO_2 (a-silica) has been researched for over a half century, with a vast amount of contradictory models for defect formation. [67]. In 2000 the NATO Science Program attempted to enclose the vast amount of differing models and results, between the East block and NATO, and within countries them-self. However, there are still many remaining puzzles to this subject. The vacancies and absorption values presented here are all from the agreed upon models after the 2000 NATO meeting. Electron paramagnetic resonance studies have been the most successful spectroscopy method for characterising the vacancies. There are about half a dozen documented vacancies in pure a-silica and ten times more when including impurities. This makes point defects in silica glass a vast subject. Understanding these point defects are of large scientific interest within electronics, fiber-optics and lasers [31, 68].

It is generally admitted that different types of irradiation sources result in similar damage to the atomic structure and optical properties in glasses [27].

Vacancies that change optical properties are often referred to as colour centres. Colour centres in SiO_2 appear more frequently in vacuum ultraviolet (VUV) spectral range, than visible light. However, they are broadband and may therefore increase absorption of visible light even though the defect is primarily UV absorbent. Figure 2.17 are the transitivity of (a) B270 and (b) a-silica glass after 350 Gy with gamma radiation [69]. Both glasses show a decrease in transmittance, which is highest towards UV. Keep in mind that B270 is the glass used in the grating.

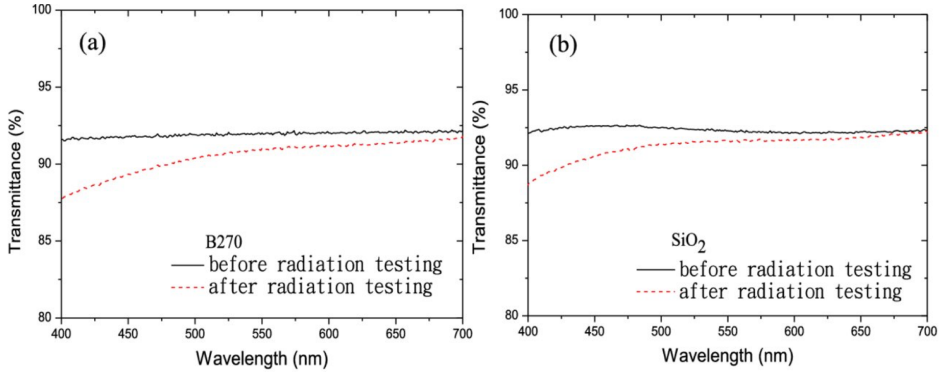

Figure 2.17: Transitivity for B270 and pure a-silica glass after 350 Gy of gamma radiation. The colour center peaks are in UV, but they impact the visible spectrum. Both glasses absorb about 7% more blue light and about 1 % more red light. [69].

The rate of vacancies introduction can be delayed by doping with heavy rear earth elements. Especially cerium is known for having high radiation resistance when doped into silica glass, this is due to Ce^{3+} ion compensation to capture radiation induces holes [28]. However, cerium doped glass are more absorbent to VUV and come with a yellow tint, and lower transitivity. Choosing radiation resistant glasses are therefore a trade-off between sacrificing initial transmission, for reduced transmission decay over time.

Vacancies in Amorphous Silica Glass

Absorption peaks in a-SiO_2 appear as broadband absorption peaks, instead of sharp spectral lines. This is due to This is due to the defects often introducing sub level in the same energy level, where the electron release photons for multiple sub level with a peak widening effect of 0.2 - 1 eV, instead of one distinct energy level [31].

Vacancies of SiO_2 fall into two categories, oxygen deficient and oxygen excess. Oxygen deficients are generally more studied as these where first found of the two, with the originally discovered colour center, the E' centre being among these defects [67]. Figure 2.18 visualises the more accepted oxygen deficient a-SiO_2 vacancies, and Table 2.3 summarises their absorption area. The most common vacancies are (a) Silicon oxygen deficient, and (B) the E'-center [31, 70].

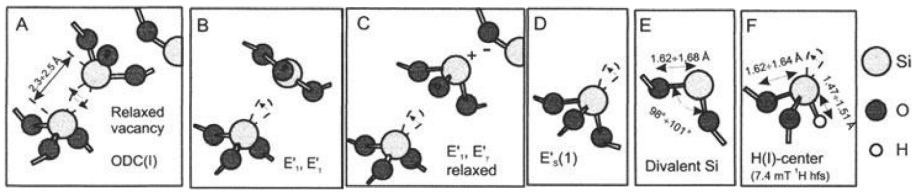

Figure 2.18: Main colour centres in silica glass, by oxygen deficiency vacancies. (A): Oxygen deficient Si-Si bond. (B,C): Oxygen vacancy with a trapped hole (E'-center). (D): Surface-type E' centre (E): Twofold-coordinated oxygen deficiency centre ODC(II). (F): Twofold-coordinated silicon with a trapped hydrogen atom - H(I) centre. [31]

Table 2.3: Peak absorption band and band width for main oxygen deficient vacansies in silica glass. All of these absorptions peaks are in the UV spectrum, but they can blend into visable light [31, 68].

		OCD(I)	E'center	$E_s(1)$ center	OCD(II)	H(I) center
Band peak	[eV]	7.6	5.8	6.1	7.6	5.0
Peak equivalent	[nm]	163	213	203	163	246
Band half-width	[eV]	0.5	0.6	-	0.1	0.4

Oxygen-excess vacancies are generally of lower intensity than the oxygen deficient counterpart, and therefore, have generally better UV transparency. Figure 2.19 visualises the more accepted oxygen excess vacancies in a-SiO_2, and Table 2.4 summarises their absorption area. The most common vacancy is (A) non-bridging oxygen hole center and (B) peroxy radical. The formation ozone molecule (E) is the most controversial of these defects, partly due to being impossible to distinguish optically, since it shares the same absorption band as other vacancies [31, 67].

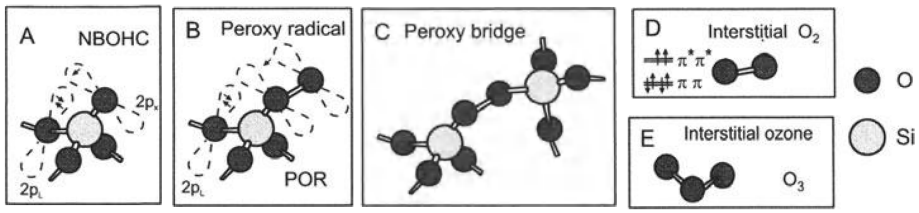

Figure 2.19: Main colour centres in silica by oxygen excess vacancies. (A): non-briding oxygen hole centre (NBOHC). (B): Peroxy radical (POR). (C): Peroxy bridge. (D): Interstitial oxygen molecule. (E): Interstitial ozone molecule [31].

Table 2.4: Peak absorption band and band width for main oxygen excess vacancies in silica. non-bridging oxygen hole centre have two absorption peaks, where 4.8 eV are the vacancy in bulk material and 1.9 eV are the surface equivalent vacancy [31, 68].

		NBOHC		Peroxy radical	Peroxy bridge	Intersteller O_2	Interstellar ozone
Band peak	[eV]	4.8	1.9	7.7	6.5	$<$6.5 eV	4.8
Peak equivalent	[nm]	258	649	161	190	$>$190	258
Band half-width	[eV]	1.1	-	0.6	-	-	1

Annealing of Colour Centres and Recovery of Optical Properties

All of these vacancies are thermodynamic unstable, and will transform to the original SiO_2 structure or another vacancy. All vacancies will by some temperature close the glass transition temperature (1060°C) become unstable and disappear. All these vacancies will become thermodynamic unstable between room temperature and 400°C [31]. This introduces time dependency as a effect in characterising optical properties of irradiated glasses [67].

Chengyue Sun et.al(2011), has modelled this annealing process for the E' centre. This is illustrated in Figure 2.20 where an E' (2) centre and SiO_2 crystall develope to two E' (1) centre. Note that this process effectively doubles the number defects [71].

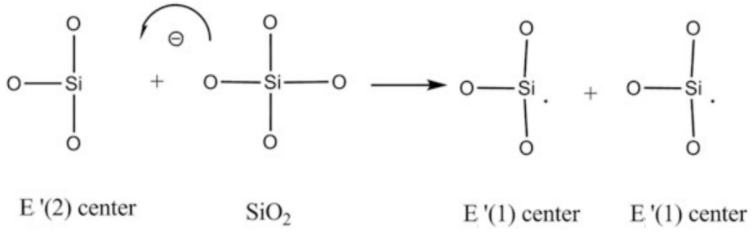

Figure 2.20: Annealing from E' (2) centre to two E' (1) centre [71]

Chapter 3

Method

This chapter describes the method applied for the simulation radiation amounts, and component testing methodology used.

3.1 Space Radiation Simulation

Radiation environment simulations were conducted with the use of the simulation software OMERE version 5.2.5.0.

Mission orbital parameters where set at as the orbit parameters in the HYPSO mission analysis report [2] and is summarised in table 3.1. Where the semi-major axis is the sum of the Earth's radius and the altitude of the satellite, which is about 6 371 and 500 respectively. Eccentricity is how elliptical the orbit is varies between 0 and 1 with 0 being a perfect sphere. The launch date was assumed 1st December 2020. Mission segment duration where set at 5 years, which is according to the requirement, detailed in the HYPSO mission analysis report [2], for mission full success.

Table 3.1: HYPSO orbital parameters.

Semi-major axis	6878.14	km
Eccentricity	0.00015	-
Inclination	97.4065	degree
Launch	01/12/2020	date

The simulation software requires an input of calculation points per orbit and the number of orbits to simulate. Number of points per orbits defines how many points in space the program must account for in its simulation. Considering the number of orbits is important, as most orbits dos not end in there same starting longitude, as the earth is rotating. Higher number of orbits and points per orbit gives higher accuracy per simulations, but increases the computational time. As a result, a trade of of simulation accuracy and computational time is necessary.

The convergence study is seen in Appendix 5.9, where one can see overlapping simulations after 50 points per orbit, and 15 orbits. Both these plots are visualised in a log log plot of ionised dose (rad) per mm Al, this is to highlight where the simulations start having overlapping results. 100 point per orbit and 30 orbits where used, as computational time wasn't a issue.

The objective for simulations were to find where the radiation fluxes are highest in orbit, to describe radiation types effects on total dose and to find how total dose is impacted by shielding and years in orbit. Two radiation simulations have been conducted, a radiation orbit flux mapping and a shield dose analysis. The orbital radiation flux mapping is conducted primarily for a visual representation of the space environment, while the shield penetration simulation is intended for calculations. In Table 3.2 are the models and adjustment used for the simulation, these where all suggested as standard.

Table 3.2: Models and adjustments in the simulation

Source	**Trapped Electron**	**Trapped Protons**	**Solar particles**
Model	AE8	AP8	ESP
Magnetic field model	Standard (Jensen-Cain)		-
Confidence level	-		80%
solar activity period	-		3.5 years
Magnetospheric cutoff model	-		Stormer

The simulation requires a geometry to simulate the fluxes on. For the purpose of the space radiation simulations a solid sphere of aluminium with an internal core of SiO_2 were used.

3.2 Components and Test Overview

Table 3.3, summarises the tests conducted and the components tested. The testing was conducted to evaluate radiation resilience on COTS components of prime importance in the HSI. Material composition and crystallinity was performed on the samples of unknown material composition. All samples where irradiated, and there were also brought a reference samples for those that were characterised at the cobalt-60 facility. The reference samples were marked with yellow tape to clearly distinguish between irradiated samples. The alternative slit from Ealing was however not irradiated. Figure 3.1 shows the samples taken to DTU. Irradiation of the sensor is excluded from this report, however, the sensor

glass and gasket are taken from this sample. Figure 3.2 show the sensor glass and gasket next to the sensor it was taken from. These two samples were removed from the sensor as they were most likely going to be removed on the flight version for the HSI, and it could, therefore, be a false negative.

Irradiated samples involved in the HSI design are stored at the SmallSat Lab for further testing.

Table 3.3: Overveiw of samples and testing.

	Irradiated objective	Grating	Slit (Thorlabs)	Sensor glass	Sensor gasket	Reference objective
EDS				x		x
XRD						x
Gamma irradiated	x	x	x	x	x	
Visually inspected post radiation	x	x	x	x	x	x
Optical characterisation	x					x
Spectral characterisation	x					x
Stored at SmallSat Lab	x	x	x			

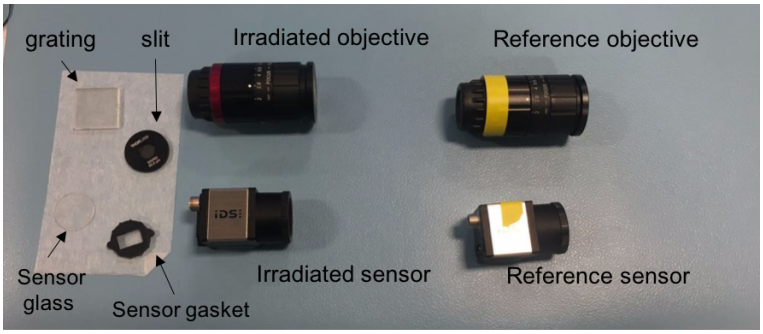

Figure 3.1: Picture of samples taken to DTU, the yellow marked are samples are references.

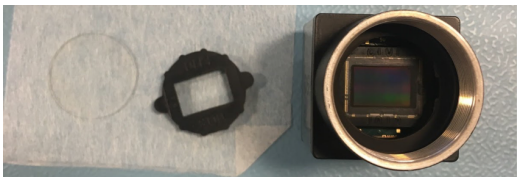

Figure 3.2: Sensor glass and gasket laying on a sheet of cloth, next is the sensor this was taken from.

Figure 3.3: Objective housing detached

3.3 Analysis of Components and Materials

A non-irradiated objective was disassembled in order to take out the lenses for chemical composition and crystallinity testing, but also to understand the design of this component. It was attempted to measure the thickness of the aluminium housing. However, the geometric complecity made this difficult, Figure 3.3 show the housing parts. It was estimated minimum a value, instead of measuring each piece individually and combining the result.

Material identification was performed with Energy-dispersive spectroscopy (EDS) in order to identify chemical composition, and X-ray diffraction (XRD) to evaluate the degree of crystallinity within the samples. The purpose of the test was to find the dominant materials for both the surface coating and substrate of all lenses, and the dominant material of the sensor components.

3.3.1 Chemical Composition of Lenses

EDS is a quantitative chemical microanalysis that analyse secondary X-rays, from a sample bombarded by electrons [72]. EDS was performed with a scanning electron microscope (SEM) (JEOL JCM 6000). The analysis was performed to detect material composition in the substrate and surface of the glass. A 15 keV electron beam and high resolution image was used to find the right area to analyse with EDS. The distance between the observed surface and the electron beam was kept at a distance of $20mm \pm 1mm$. Finding focus on glass was difficult because of the lack of structures to focus at.

SEM and EDS requires the material to be conducting electricity. Glasses are electronic insulators and usually requires coating the material in carbon, however it was checked if this worked without carbon coating, and the analysis performed successfully without. There were charge build-up on the glass samples, causing the sample to move slightly and giving rise to white lines in the picture.

The EDS analysis was performed as spot analysis, and was performed on each lens

un-honed, meaning it was with surface treatment if it had. Later the 1st lens was honed down to what was believed under the surface treatment and tested again with EDS.

3.3.2 Crystallinity of Lenses

XRD was used to study crystallinity degree and chemical composition. The technique used a X-ray beam directed on the sample over a variation of 180 °, while measuring absorbed, scattered and transmitted X-rays. The analysis provided a diffractogram of intensity over angle. Sharp peaks represent a distinct crystallography and a chemical substance, no distinct sharp peaks indicate amorphous structure [72].

XRD was performed on the 1st and 6th lens, the four other lenses was not tested due to geometric constraints. XRD was performed on both surfaces of these two lenses, neither of these surfaces are perfectly plane. This is reduces the quality of the analysis, but it was the only method of testing the surface treatment. The rear lens was afterwards crushed into powder and re-analysed to observe the structure of the substrate.

3.4 Radiation Exposure Test

The accelerated radiation exposure test is conducted to simulate radiation on the test samples by using gamma radiation from a cobalt-60 source. The document in Appendix 5.8 was sent DTU Risø in order to conduct this test. This document was written by this author in collaborated with students Tord Hansen Kaasa, Henrik Galtung and Tuan Tran from the HYPSO mechanic team. The tests where conducted by the author in collaboration with student Marie Henriksen. The sensor of the HSI camera was also tested, but is not included in this report as it was considered out of scope of the test.

3.4.1 Equipment

Table 3.4 lists all equipment and equipment quantity used during the test procedure.

Table 3.4: Equipment list

Equipment	**#**
Cobalt-60 gamma cells (Radiation Chamber)	1
Computer with DUNE (software)	1
Dark room	1
Temperature and humidity sensors (DTU)	1
Optical breadboard	1
Stable light source, incl. power supply	1
Diffuse target (A4 paper in frame)	1

3.4.2 Radiation Exposure Set-up

The test chamber was an open space within a lead cylinder where samples could be placed, as seen in Figure 3.4. The cylinder was then lowered to the radioactive cobalt-60 source in order to receive the radiation exposure. The amount of radiation exposure is dependent of the radioactivity of the source, distance between source and sample, and time. Radioactivity and distance is considered fixed variables, making the chamber emit 6.4 Gy/min (calibrated 2014). Radiation dose values vary slightly within the chamber, with the highest doses in the center.

It should be mentioned for future testing that the chamber is equipped for irradiation powered electronic equipment, with a wired connection through to top of the chamber. This was not pursued during this set-up but could allow for dynamic testing of the equipment during the irradiation.

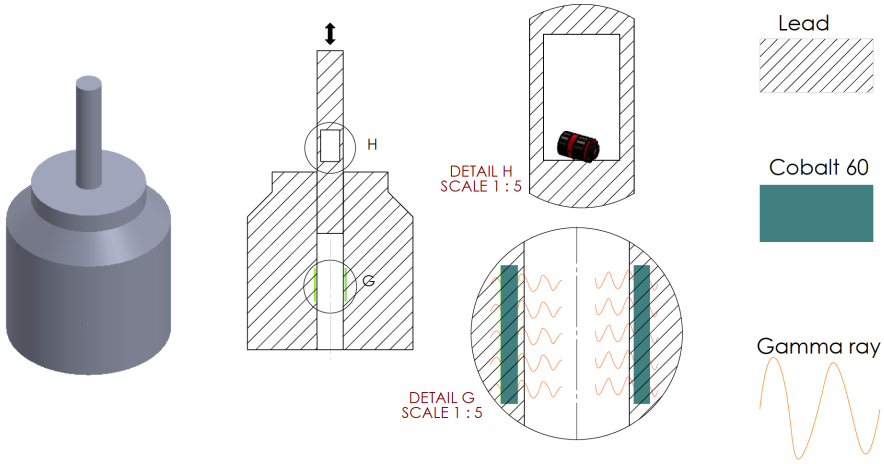

Figure 3.4: Illustration of the cobalt-60 exposure apparatus, with focus view H of the test chamber and G of the cobalt source. During radiation exposure the test chamber will be lowered level to the cobalt-60 source. Illustration drawn in Solidworks

Table 3.5: The radiation exposure timetable

Set Dose [Gy]	Time [min:min/100]	Time [min.s]	Total time [min.s]	Total radiation dose [Gy]
5	1:51	01.30	01.30	5
5	1:51	01.30	03.00	10
10	3:07	03.04	06.04	20
10	3:07	03.04	09.08	30
10	3:07	03.04	12.12	40
20	6:18	06.10	18.24	60
20	6:18	06.10	24.34	80
20	6:18	06.10	30.44	100
40	12:42	12.25	43.09	140

3.4.3 Health and Safety

Ionising radiation can cause serious damage to the human body. Therefore, the cobalt-60 cells are placed behind think lead shielding. According to the professors at DTU, gamma rays will also ionising oxygen to form small consentrations of ozone, which is poisonous gas and should not be inhaled.

A radiation test facility is considered safe to work within as long as one follows the health and safety regulations. However, extended presence close to the gamma cells should be limited. In advance, there was conducted a HSE study on NTNU Risk Manager. The risk study is in Appendix 5.7. The personnel conducting this test were wearing Geiger counter (radiation exposure measuring equipment) during all time in the radiation lab.

3.4.4 Visual Inspection

Between every dose of radiation exposure, the samples were photographed and observed visually. Photographs were taken with a camera phone with automatic settings and various backgrounds. The sensor rubber was also physically inspected by squeezing by hand to look for changes in stiffness and viscoelastic behaviour.

3.4.5 Optical Characterisation of Radiation Exposed Objectives

Radiometric characterisation was performed to detect any changes in transmission of light through the lenses. In the test both a objective and a sensor was irradiated and tested with a reference (non irradiated sample), however this report only covers radiation on the objective. In addition, a reference objective tested with reference sensor will also be compared, to detect any changes not due to radiation. The radiometric characterisation was performed prior to the first radiation dose and after each dose.

Transmission of light through the lenses in the objective is measured by taken images of a white plane illuminated by a stable light source and comparing these over increased radiation exposure. To achieve this one needs high control over light sources and a rigid construction for holding the objective at the same position for each characterisation. Normal lamps produce flickering light, and therefore a thermal lamp was used, which is non flickering. The optical characterisation set-up can be seen in Figure **??**. The lab worked as a dark room when the light was switched off. Minor light sources were still present, such as small lamps indicating equipment was on, but these were assumed irrelevant compared to the light from the stable light source, and deemed negligible when wrapping a scarf around the sensor during dark current measurements. The light was aimed at a diffuse target which was a stack of white papers held in-place by four posts and a frame without glass. The lens objective holder was mounted in the opposite side of the light source, and pointed towards a high illuminated area on the diffuse target. Test image taken and adjustments were made until the lamp illuminated the full field of view, then the position of the lamp and lens objective holder then fastened properly.

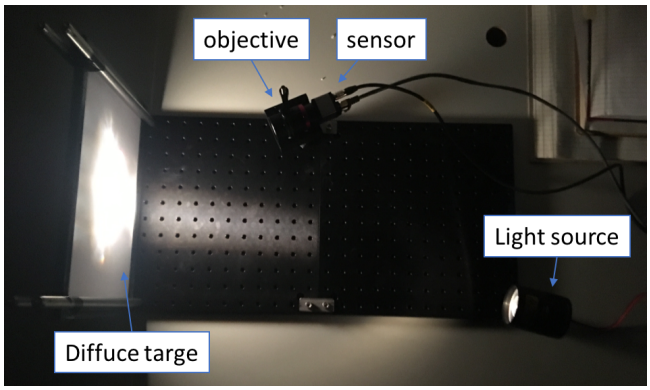

Figure 3.5: Set-up in dark room. Highlighting the objective under characterisation while a sensor is taking the images.

Figure 3.6: The f number was set slightly above 2.8 in what looks like f3

The objective was adjusted and locked to focus on infinity (no final focus point) and f-number at 2.8 for both the ref- and rad-objective. However, it was noted after the first radiation dose (after series 2) that the f-number for the irradiated objective was not perfectly set at the f-stop-number 2.8, but slightly higher, as can be seen in figure 3.6. A small change in f-number gives a small change in incoming light to the sensor. A higher f-number gives a smaller aperture, which means the irradiated objective would make the sensor receive slightly less light than when using the reference objective. The maximum response for the sensor is 4100 counts, and the maximum count in the middle line approximately 3000 counts after parameters were set. There were brighter areas above and below the middle line which is why a count of 3000 was selected. The main parameters used in this characterisation was an exposure time of 0.5 ms, at a frame rate of 10 fps.

The focus and aperture of the objectives were checked before each characterisation. The objective was placed in the same position as accurately as possible for every characterisation. The position of the objective and sensor was tuned by trying to have the sensor levelled, a leveller could be used in future characterisation for more accurate positioning. For analysis purposes, a single line in the image, chosen as the middle line, will be compared between the picture series. At least 30 images were collected, and at least one of them inspected by showing the image and plot the middle line, to make sure the data collection was successful. Note that the lens objective holder slipped out of position after the final irradiation dose. It was moved back in the right position, however there is a chance that the position is somewhat altered compared to the base position.

3.4.6 Spectral Radiometric

This characterisation follows the same procedure as for radiometric, however a hyperspectral camera was uesd instead of a normal imaging sensor to detect changes in transmissivity over different wavelengths. The HYPSO project's working HSI was used for this characterisation, placed laying behind the objective, as shown in Figure 3.7. The characterisation was done for both the reference and 140 Gy irradiated objective, and the transmission through the two were then compared.

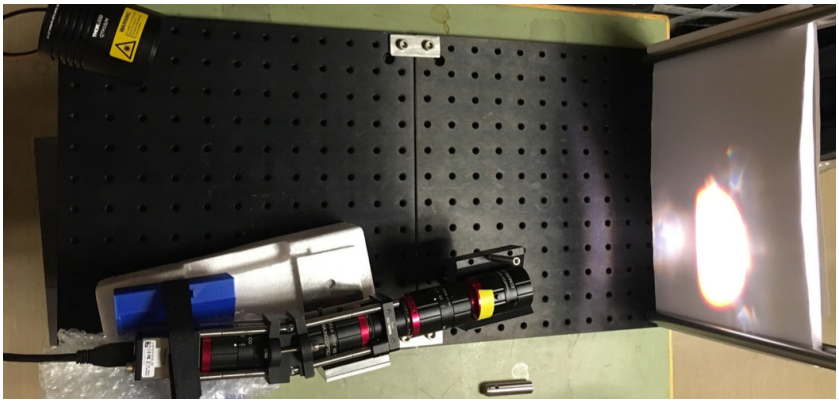

Figure 3.7: A HSI placed behind the objective to characterise.

3.5 Total Transmission Loss Analysis

The percentage of total lost light was described as the product of light lost in each objective. This is illustrated in Figure 3.8 and described in equation (3.1). I is intensity and T is relative loss in transitivity.

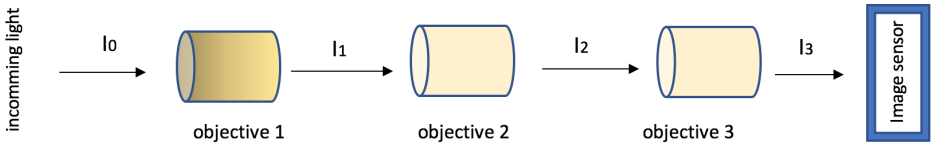

Figure 3.8: Illustration of the three objectives, which may have discoloured do to radiation and subsequently reduced optical transmittance.

$$I_3 = T(objective_3) \cdot T(objective_2) \cdot T(objective_1) \tag{3.1}$$

One can describe the transitivity loss for each objective as a function, where T(Gy$_\gamma$) is the tested transmitivity loss and Gy$_{objective}$ is the exposure dose in space of one objective.

Chapter 4

Results

The chapter is structured space radiation simulations, with material identification and testing of irradiated samples.

4.1 HYPSO Orbit Radiation Simulations

The radiation flux simulation along the orbit are displayed in Figure 4.3. The radiation flux over the polar regions and the South Atlantic Ocean is in the order of 10^{-4} Rad/s (10^{-6} Gy/s). Most of the orbit experiences fluxes of 10^{-13} Rad/s (10^{-15} Gy/s).

Simulation of different sources penetration-impact on aluminium is displayed in Figure 4.1 and Table 4.1. The total dose (black) is in the order of 10^6 rad (10^4 Gy) at 0 mm Al, and is falling exponentially the first 5 mm, after 10mm the total dose converge towards a flat line. Trapped electrons are the predominant radiation source between 0 and 6 mm, but goes toward zero at higher thicknesses. At 6 mm there is a point where trapped electrons, protons and solar photons intersect. After 6mm the dominant radiation source is trapped protons.

Table 4.1: Total dose at 5 year orbit duration

Aluminium shielding [mm]	0	1	2	3	4	5	6	10
Penetrating dose [Gy]	$8.3{\cdot}10^3$	60	19	8.5	4.7	3.2	2.5	1.5

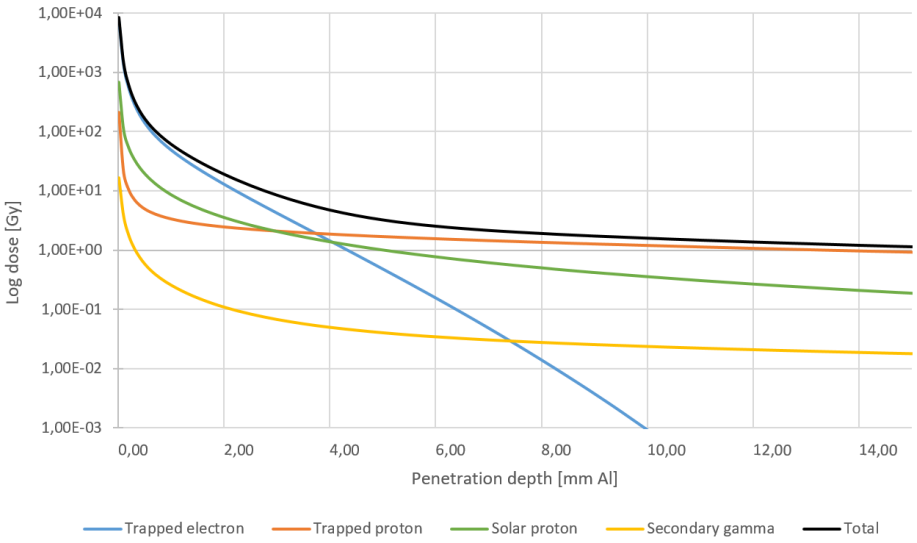

Figure 4.1: Simulation of ionisation depth in aluminium for protons and electrons from radiation belts and solar

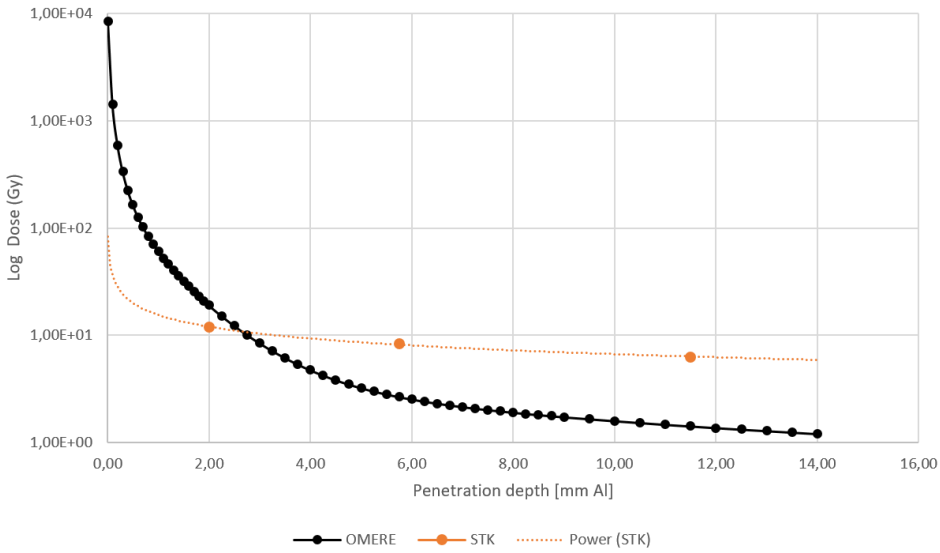

Figure 4.2: Comparison between the OMERE and STK simulations, both show total simulated dose. There are only 3 levels of shielding in the STK analysis, but over 50 in the OMERE simulation. Excel power function was used to the trend in the STK simulation.

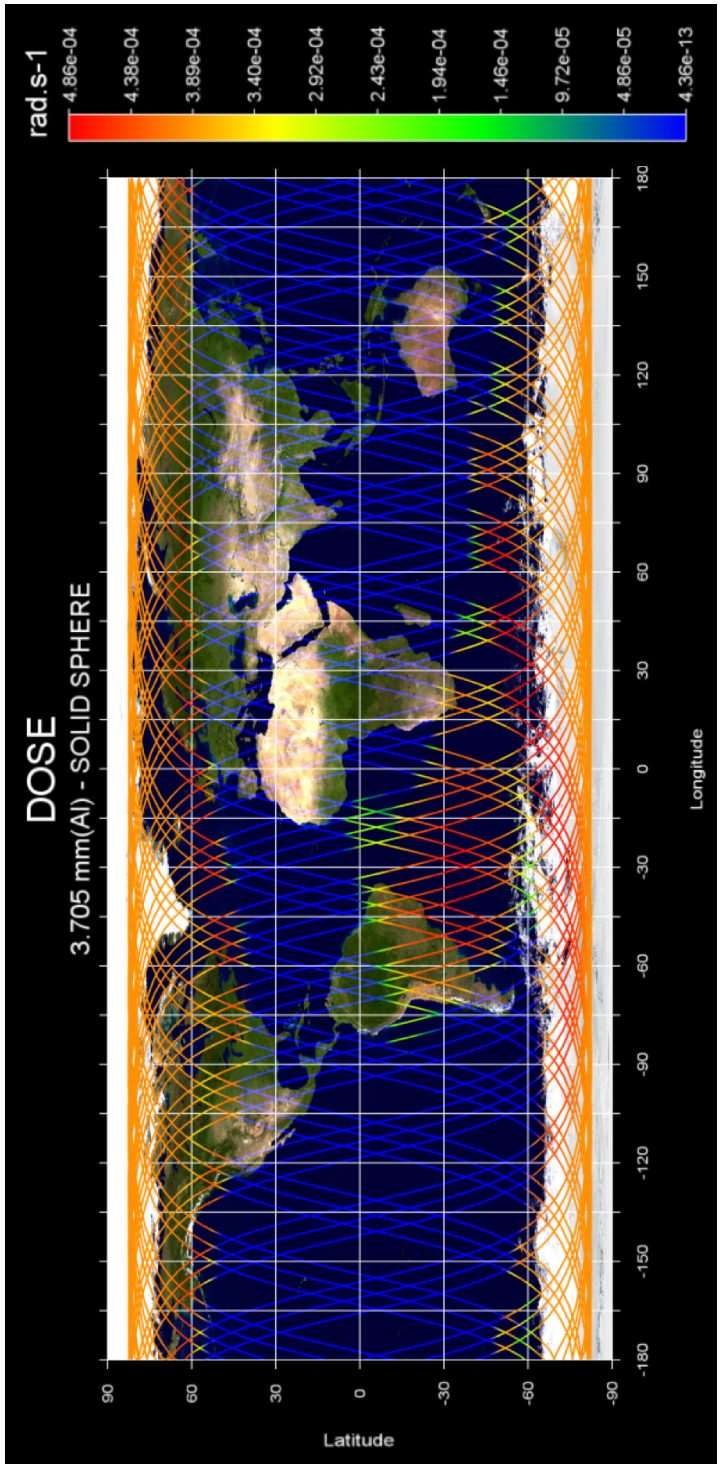

Figure 4.3: Here one can see fluxes of $10^{-4} Rad/s$ over Brazil and polar regions, and $10^{-13} Rad/s$ in all the blue orbits.

4.2 Component Analysis

Disassembling the objective revealed six lenses, where four of these were fastened together with a chemical bonding material. The aluminium housing was comprised of several parts which had a complex geometry, however the measured minimum shielding thickness appeared to be approximately 3 mm. Figure 4.4 gives a visual representation of the lenses inside the objective and the minimum shielding thickness.

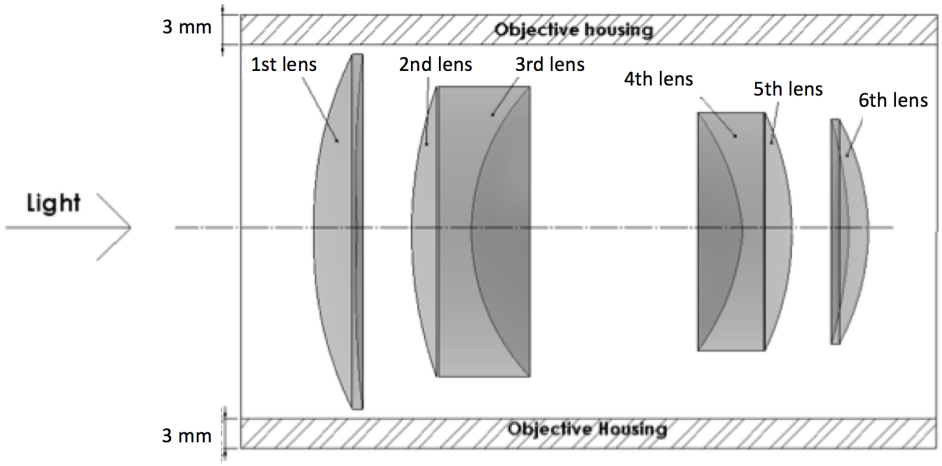

Figure 4.4: A cross-section illustration of the objective, drawn in Solidworks. This illustrates the shielding thickness of the objective housing, and the lens numbering system used.

Lens Chemical Composition

The EDS results for the glasses with surface treatment are given in their complete form in Appendix 5.10. Major quantities of F, Mg, O and Si along with varying quantities of O as well as minor quantities of Tantalum, Titanium and Aluminum were found within the analysed samples. Presented in Table 4.2 are the measured amounts of F, Mg, O and Si. The percentage reported does not add up to 100% due to the exclusion of other substances found in the test. This is because the prime focus was to find main materials. In Appendix 5.10.6 one can see the 6th lens has a registered emission line of Tantalum adjacent to Si.

Lens Crystallinity

XRD was performed to study the crystallinity of the lenses. In Appendix 5.10 one can see the XRD results for the 1st and 6th lens on both sides. For the first glass, one can see a sharp intensity peak at 36°, and a smaller at 43°, this is indicate a crystalline surface. The back surface of this lens has no distinct peaks, as a amorphous material. The 6th lens has both a broad peak at 27°, and a sharp but less intensive at 36°, appearing somewhat crystalline. While the back facing surface has one distinct sharp peak at 35°, appearing crystalline.

The XRD result for the powdered 6th lens is seen in Figure 4.5. This has a smooth wavelike result, with a broad, but distinct peak at 28°. This indicate that the material is amorphous.

Table 4.2: EDS results for all glasses, of both substrate and surface treatment.

	1st lens				**2nd lens**			
element	O	F	Mg	Si	O	F	Mg	Si
mass %	14	54	18	3.5	10	60	23	5
atomic %	26	70	18	3.5	13	63	20	3
	3rd lens				**4th lens**			
element	O	F	Mg	Si	O	F	Mg	Si
mass %	30	36	7	11	9	63	18	6
atomic %	35	34	6	7	12	67	15	4
	5th lens				**6th lens**			
Element	O	F	Mg	Si	O	F	Mg	Si
mass %	17	56	18	9	12	52	10	3
atomic %	21	58	14	6	18	65	10	3

Table 4.3: Stoichiometric between MgF and SiO

	1st lens	2nd lens	3rd lens	4th lens	5th lens	6th lens	1st lens honed
Ratio: Mg : F	1 : 3	1 : 3.2	1 : 5.7	1 : 4.4	1 : 4.1	1 : 6.5	1 : 3.3
Ratio: Si : O	1 : 5	1 : 4.3	1 : 5	1 : 3	1 : 3.5	1 : 6	1 : 7.6

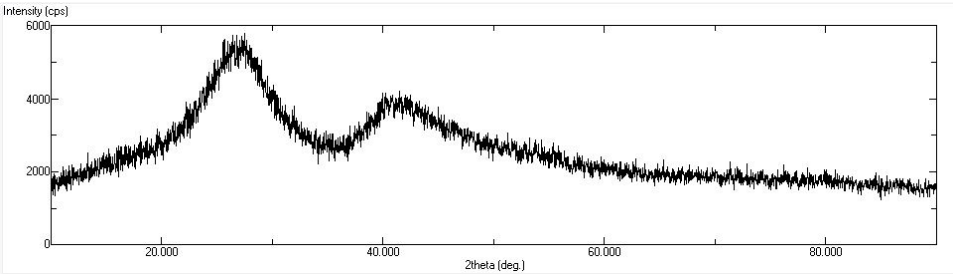

Figure 4.5: XRD result for the powdered 6th lens.

4.3 Radiation Exposure and Optical Characterization

Visually one could see a yellow tint in the objective after the higher doses of radiation, this is seen in Figure 4.6 where the irradiated objective is compared to the reference. No differences could be seen on the sensor, grating nor slit. However, the glass detached from the sensor got a few white particles on the surface that used to be squeezed into the rubber piece. In Figure 4.7 one can see pictures of the detached glass taken after several exposures, there are more white particles after higher radiation. Hand squeezing the detached rubber piece did not reveal any changes in stiffness, nor could any visual changes be seen. Table 4.4 summarise the visual observations.

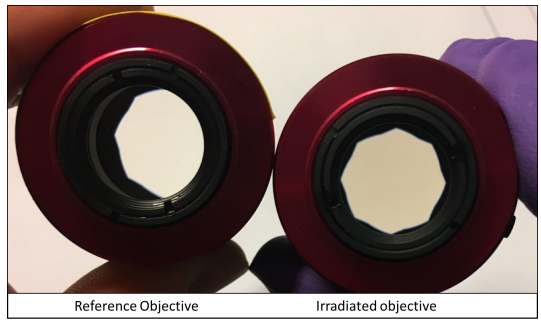

Figure 4.6: Picture of the reference objective next to the 140 Gy exposed objective.

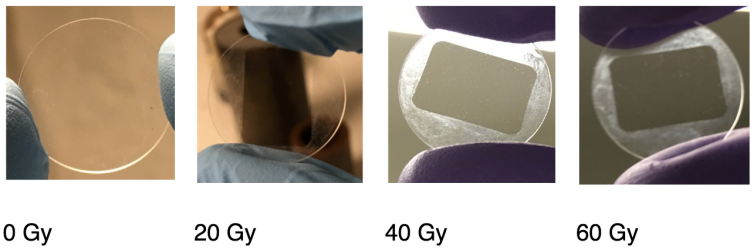

Figure 4.7: Front glass of the sensor after increasing amounts of radiation exposure.

Table 4.4: Summary of visual observations

Sample	**Visual observation**
Objective	The colour of the glass became gradually more yellow
Sensor	Nothing visually apparent
Grating	Nothing visually apparent
Slit	Nothing visually apparent
Detached glass	White spots appearing on the surface pressed against the rubber piece
Detached rubber	Nothing physically or visually apparent

4.3.1 Radiometric Characterisation

The raw data obtained from the radiometric results are seen in Figure **??**. (a) the irradiated objective has a significant intensity decrease for every series of increased radiation exposure, the tenth series appears to be right shifted. The reference, which is an un-irradiated sensor and objective, is keeping a steady intensity for all series, but is left shifted in the tenth series. The shift in X-axis corresponds with when the objective was unintentionally rotated. On the irradiated objective, the sensor is mounted 180° to the breadboard, which make a leftward rotation appear in the opposite direction.

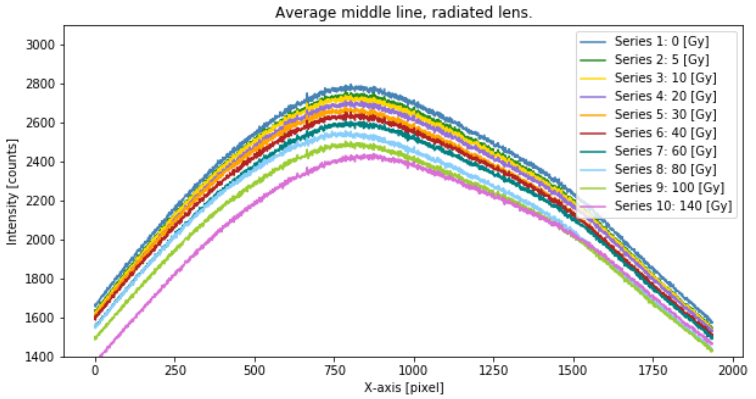

Figure 4.8: The observed light through the irradiated objective is less intense for each accumulated radiation dose, the 10th series is right shifted

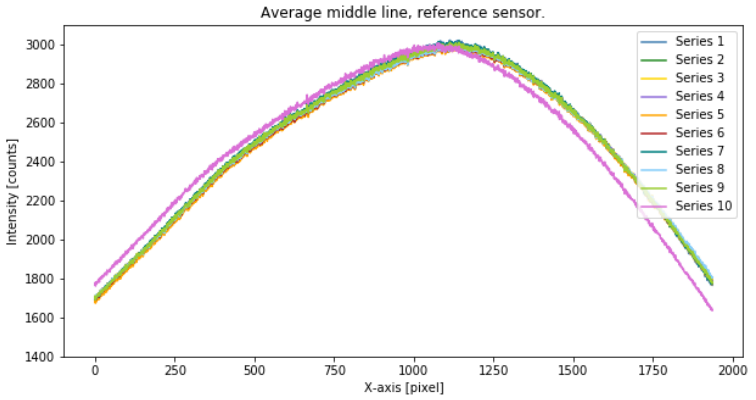

Figure 4.9: The observed light through the reference objective is equally intense for each series, the 10th series is left shifted

Relative transitivity for the objective is plotted against radiation dose in Figure 4.10. The data points are calculated by dividing the intensity difference on initial intesity. Intensity are measured from the average top point in Figure 4.8. Using average top point is intended to remove the impact of faulty pixels. From a linear trendline it is found a transitivity decrease of 0.10% per Gy with a reliability off 0.99.

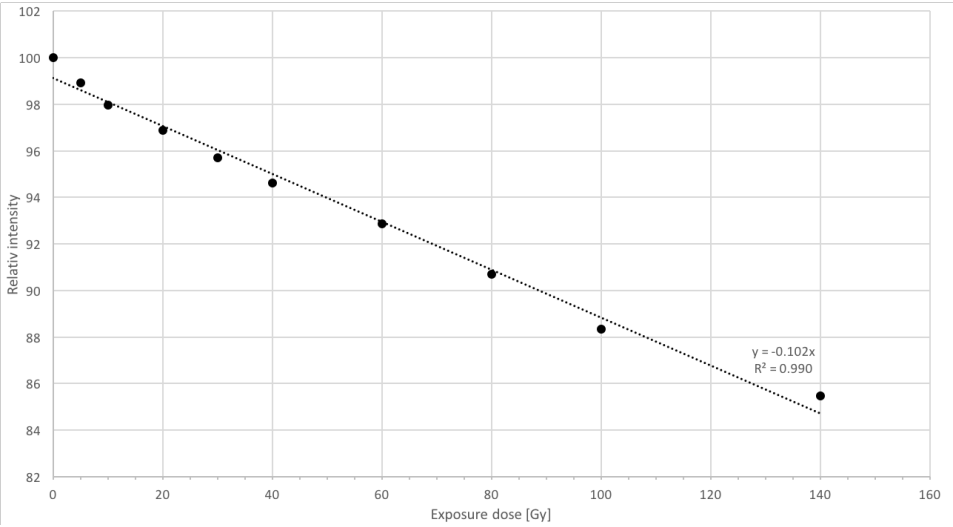

Figure 4.10: Relativ intensity fall per ionized dose. The percentage is calculated by dividing on initial intensity.

In table 4.5 one can deduce that the radiometric test imminently after 140 exposure is 19% loss and after 15 days at room temperature it is 21%. This is intended for observing signs of annealment

Table 4.5: Radiometric comparison with 15 days post radiation

	Pre-radiation	**Post radiation**	**15 days post radiation**
Reference objective	3022	3008	3027
Irradiated objective	2796	2441	2405
delta intensity	226	567	622
% difference	7.48	18.8	20.5

4.3.2 Spectral Radiometric Characterization

Figure 4.11 is the spectral comparison between the two objectives, taken with a HSI. One can see a general decrease in intensity for the irradiated objective. Figure 4.12 present the percentage difference. Here one can see a top point of 25% intensity loss at around 450 nm. Between 450 and 800 nm there is a gradual fall to 5% intensity loss, while between 400 and 450 it is sharp. This sharp fall corresponds to the raw data going towards zero intensity at 400 nm. 400 nm is at the extreme for the HSI capabilities.

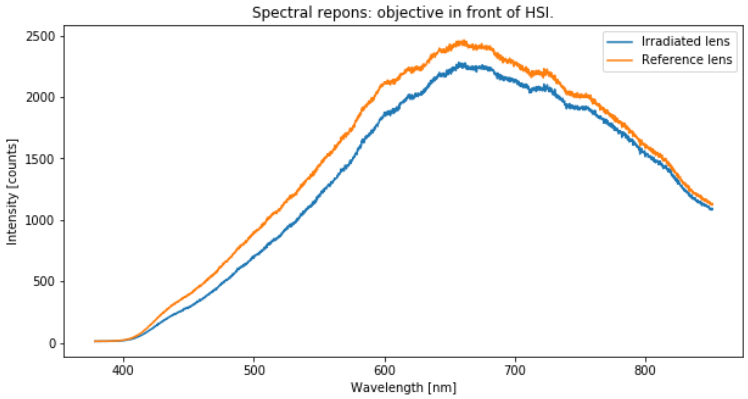

Figure 4.11: raw spectral data between the reference and irradiated objective.

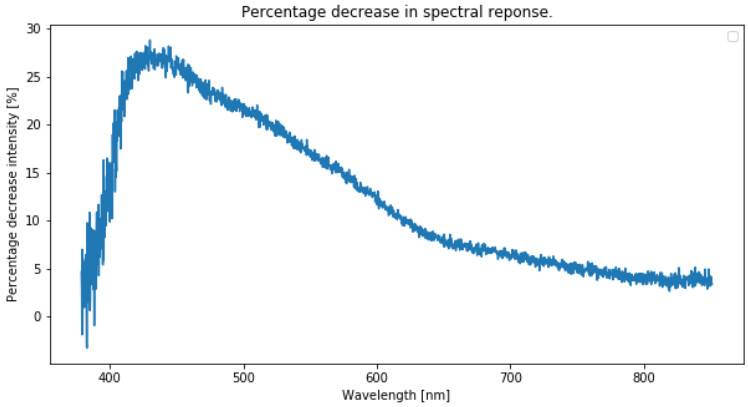

Figure 4.12: Percentage difference in intensity per wavelength on the irradiated and reference objective. The percentage is calculated by dividing on intensity of reference objective.

4.4 Total Transmission Loss Analysis

In Section 2.1.5 it said that there is a minimum thickness of 3 mm around the objectives. And in Section 4.2 it is estimated a minimum thickness of 3 mm aluminium from the objective themselves. This results in a total of 6 mm shielding thickness, but this is not the case for the first objective as it has an exposed face to the front. With a 6 mm shielding value, one can read the radiation dose value to be 3 Gy in Table 4.1. By multiplying the 2.5 Gy with transitivity decrease of 0.10 % Gy one gets a 0.3 % intensity fall over both objective 2 and 3.

Chapter 5

Discussion and Conclusion

This chapter presents a discussion of the results obtained from the material identification of the optical components, impacts of radiation environment on the satellite, radiation testing.

5.1 Space Radiation Environment

The satellite will be subject of solar, trapped and galactic radiation. However, the standard for space environment claims that galactic radiation is primarily a concern to humans and electronics. This is a bit peculiar, due to galactic cosmic rays being 85% protons [47]. Excluding galactic radiation as source is likely a common simplification.

The satellite is within the reach of the internal radiation belt, and is estimated to receive high doses of protons and electrons. As described in Section 2.4.1 the sun will constantly emit protons and electromagnetic radiation up to low energy X-ray. It is doubtful if these X-rays are energetic enough to ionise the glasses in the objectives. When considering the shielding, the X-rays are definitely not able to ionise said glass. However, the irregular solar flares and coronal mass ejections will irradiate the spacecraft with electrons, protons and electromagnetic radiation up to gamma. Particle radiation form solar flares/coronal mass ejections are also more energetic than solar wind. The higher energy particles will penetrate deeper, and cause more ionisation/atomic displacement in the glass. Solar flares and coronal mass ejections are random. This is a problem when projecting radiation over time. As one month with multiple solar flares will have many times the radiation flux as a month without.

Alpha particles are often overlooked as they are the easiest to shield against. However, the unshielded lens will be ionised by this source, and alpha particles should therefore not be overlooked. Neutron radiation are negligible however, since almost all decay before LEO.

The largest portion of the radiation comes from the amount of time spent over the polar cups, where the satellite is more exposed. The simulations in Figure 4.3 confirm this by showing a considerable larger flux in polar regions, as well as over the south Atlantic Ocean.

The simulations are modelled in order to calculate exposure form trapped electrons and protons, and a average solar protons. Secondary photons produced via Bremsstrahlung are also modelled, these photons should be X-ray [28]. The dose at zero shielding is at staggering 8.3 kGy, and one has to ask themselves if this is reality? The origin of this dose is predominantly electrons, and this particles are annulled rapidly, as supported by Section 2.3.1. It is interesting to compare the simulation in OMERE to the one STK simulations, OMERE is dedicated to only space radiation studies, while STK is used for a wide variety of space calculations. The adjustments in this simulation are kept standard/suggested by OMERE, one can argue that standard adjustments in a dedicated software might be somewhat accurate. The extent of adjustments between the two simulations are not compared. The correct value may probably lie in-between these answers.

5.2 COTS Component Composition

It was assumed a 3 mm shielding thickness in the objective housing. This was rought minimum estimate, but most of the housing parts are thicker than this.

Overlapping top points from differing elements is generally a challenge in EDS analysis, and requires experience to do correctly. The spot analysis of the 1st and 6th lens have an indistinguishable Tantalum and Silicon peak, with a reported value of twice as much Tantalum as Silicon. However, Tantalum has several emission lines at 1.770, 1.712, 8.146 and 9.343 keV [**?**]. And the 9.343 keV is not distinguishable, but the 8.146 keV emission line is, but it is a small peak, and cannot support that this emission line is predominantly Tantalum. Lower amounts of Tantalum should not be ruled out.

All tests revealed between 3 and 10 mass % carbon, this is not reported as it is more likely a contamination than a substance in the glass. This contamination is probably the reason the EDS was successful without coating the sample in carbon or gold, which is in theory required for EDS testing of insulating materials [72].

There is a trend among the EDS results to have a ratio of F/Mg atom between 3 and 6.5, this higher than the stokiometric ratio is 2:1 for MgF_2. Similarly, for O/Si atom of between 3 and 6, and the relationship should be 2:1 for SiO_2. This is enlarge due to the EDS being over sensitive to lighter materials, but also the other heavier elements that are mixed in the glass will take the space of the cation.

In retrospect, it should probably have been conducted more spot analysis or even better map the whole frame, to achieve higher accuracy and have a reference for precision. However, the goal is to find the main components of the lenses and not a qualitative analysis of all elements in the glass. This is the case for XRD as well, where all glasses should have been crushed into powder and tested for crystallinity. However amorphous silica glass is the most commonly used glass, so one can assume all glasses are amorphous [28].

5.3 Radiation Exposure and Optical Characterisation

Most of the testing was dedicated to the objective. This was both due to this component taking a larger part of the HSI volume, and testing constraints. Characterising irradiated components with incorporating them into a functioning HSI, would be an ideal method to test radiation induced damage. But this could not be done, due to it only existing one HSI camera for the most part in this study.

Objective

As reported in Section 2.3.3 gamma rays from Cobalt-60 will displace atoms via the Compton scattering, but is not energetic enough to knock secondary atoms. Most of the radiation would be ionising. The different radiation types will produce similar colour centres [27]. And the test with gamma is therefore presentable for the other types. The visual observation reveal a yellow tint on the glasses in the objective, this is as according to the theory on colour centres on SiO_2, but is not as brown as feared. The colour is explained by free electrons in the material, these electron change the optical behaviour from very transparent to semi-transparent by absorbing a fraction of the energy of the incoming light. The colour of the glass is a result of the colours that are most absorbed. Figure 2.17(b) for colour centres are somewhat constant with the spectral radiometric result in Figure 2.4. The colour centres formed within are a combination of several defects. With primarily absorption bands in the UV region that broadens over to visible light. Annealing of colour centers make this test

Slit

There were no visible changes to the Thorlabs slit after radiation. The alternative slit from Ealing could be prone to gas formation underneath the surface, form protons. This could be very serious, possibly worse than the colour changes in the glass. The Thorlabs slit is seen as a safer material choice as it is not made of a non-transparent substrate. Whenever the protons are energetic enough in this orbit and with this level of aluminium shielding is, however questionable [22]. This can be simulated in OMERE, but these simulations where outside of the scope of this task.

Grating

A method for characterising the grating was newer established. This is due to there only being one HSI for the most part in this study, and it was prohibited to change parts within this. Figure 2.17 show the radiation induced absorption from cobalt-60. The vacancies produced in here would largely be uniformly distributed in the material, and it is not seemed to have an effect on the diffraction. Althought it is probably safest to perform a test, with switching in irradiated grating to a functioning HSI.

The grating is also well shielded in a box of at-least 7 mm aluminium in every direction, so the radiation impact of would be small.

Characterisation Set-Up

The optical breadboard worked well and there were no problems relocating it to DTU Risø. However, all the screws were mounted in a way where it is easy to rotate the stand by mistake. This happened during the last characterisation. The lens objective holder was adjusted back to a similar position as previously, it was rotated by comparing the images until it was in a reassembling position. Future work with this breadboard should have this in mind. The radiometric results on the reference lens and reference objective show minute changes in counts, and all the series except the 10th overlap each other. By this one can see that the set-up is fairly stable between each series, and this indicates that the sources of error due to the set-up are small. When using the set-up in combination with the HSI to obtain spectral data, the set-up seemed to work fine. There is, however, uncertainty in whether this method is good enough for characterising radiation effects on the different wavelengths, particularly in wavelengths close to ultraviolet.

Sources of Error

The following list contains the perceived sources of error encountered during the testing procedure and the characterisation:

- f-number not set as precisely as it should be.
- The dark room was not entirely dark, with light sources from instruments and pc-screens.
- Ambient humidity changed from about 23% at beginning of test to 19% towards the end.
- The test parts could have been polluted due to cleaning restrictions of the objectives.
- Visual inspection was done with varying background and camera settings.
- The radiation dosage are dependant on distance from the sample and the radiation source, therefore there are minor gradients of radiation exposure within the radiation chamber, with max being in the center.

5.4 Total Transmittance Analysis

Combing the measured transmission decrease with the space radiation simulations proved difficult and it required a lot of assumptions. When assuming 6 mm shielding around the lenses in an objective one can find a transmission decrease of 0.3 % for two objectives. When applying the STK simulation instead, one would get 3 times higher intensity fall as the value in Table 2.2 is approximately three times higher. However, this simulation hint towards a significantly lower dose for the front objective, as the power function displayed an e^{-2} lower dose at 0 mm.

he transmission of blue light through the HSI is probably twice or three times as low as red light. This is evident from the theory on colour centers in Section 2.5.4 and the spectral data in Section 4.3.2. This could make measuring certain algae types more difficult, and

the result less consistent over time. One can implement a cerium-doped glass window in front of the HSI. cerium doped are highly radiation resistant, but this would reduce initial transmission as these come with a yellow tint. The benefit would be highly constant measurements.

TAn alternative measure of making the data contestant for the oceanographers would be to implement an algorithm to smooth the hyperspectral data. One can take advantage of the HSI great capability to identify specific absorption peak. If monitoring a stable absorption peak, any decrease in this signal should be of radiation on the lenses. This could serve as a method for onboard radiation calibration.

5.5 Future work

- The HYPSO project should test the irradiated grating in the HSI to see if any changed has occurred to the diffraction.
- The radiation effects on the electrical systems of the payload should be examined.
- Real optical degradation can be quantified by observing the rate of intensity loss on a known reference absorption line in the atmosphere. It is therefore suggested that after several years of hyperspectral data are acquired in space one can start to reexamine this thesis in comparison to optical data. From this one can implement an algorithm to actively adjust the hyperspectral data for optical degradation. Performing such an algorithm would make the hyperspectral data appear more consistent over time. This task could be the outline of a PhD thesis.
- The space radiation simulations should be looked over with an expert in this field. This would improve the model and be useful for researching electrical errors on the CubeSat.

5.6 Conclusion

The work in this report presents the results from a study of the space radiation environment, as outlined in 1.3 Problem Statement. Radiation induced optical degradation for all non-electrical components of the HyperSpectral Imager was studied in regard to space radiation conditions. Special emphasis was made on the objectives as it is the main optical component. After exposing the objective to 140 Gy with gamma radiation and performing optical characterisations an optical degradation of 0.1 of the transitivity per Gy is observed. This degradation is due to a family of vacancies in amorphous SiO_2 called colour centres, this makes the glass more absorbent to shorter wavelengths of visible light. The camera will therefore be less reliable to detect the ocean signatures in the blue end of the spectrum, compared to the red. The optical testing techniques were largely successfully in describing the optical changes in the components and is recommended for similar projects.

Bibliography

[1] Lab NS. Hyper Spectral Imager for Ocenaograpic Applications;. Accessed 11th April 2019. Available from: https://www.ntnu.edu/ie/smallsat/mission-hyper-spectral-camera.

[2] Mariusz Grøtte. Mission Analysis Report; 2019. HYPSO internal document.

[3] Ingvil Snfugl TIF, Srensen AJ, editors. AMOS Annual Report. NTNU. Norwegian Centre of Excellence; 2017.

[4] Toorian A. CubeSat Standard; 2004.

[5] Wertz JR, Everett DF, Puschell JJ. Space mission engineering: the new SMAD. vol. 1. Microcosm Press Hawthorne, CA; 2011.

[6] NASA. CubeSat 101; 2017.

[7] University of Saint Louis. CubeSat Database; 2019. Accessed 22.04.2019. Available from: https://sites.google.com/a/slu.edu/swartwout/home/cubesat-database.

[8] Langer M, Bouwmeester J. Reliability of CubeSats-Statistical Data, Developers' Beliefs and the Way Forward. 2016;.

[9] Lab NS. Requirements HSI SmallSat;. Internal.

[10] Berghmans F, Brichard B, Fernandez AF, Gusarov A, Van Uffelen M, Girard S. An introduction to radiation effects on optical components and fiber optic sensors. In: Optical waveguide sensing and imaging. Springer; 2008. p. 127–165.

[11] Lu G, Fei B. Medical hyperspectral imaging: a review. Journal of biomedical optics. 2014;19(1):010901.

[12] Bakken S. Dimensionality Reduction and TargetDetection in Hyperspectral Remote-Sensing. NTNU; 2018.

[13] Jiang Z, Yu Z, Yu Y, Huang Z, Ren Q, Li C. Spatial resolution enhancement for pushbroom-based microscopic hyperspectral imaging. Applied optics. 2019;58(4):850–862.

[14] Lab S. NTNU Lightweight Hyper Spectral Imager (HSI) - Product Specification. NTNU; 2019.

[15] Sigernes F. Pushbroom Hyper Spectral Imager version 6 (HSI v6) part list; 2018. Internal document.

[16] Optics E. 50mm C Series VIS-NIR Fixed Focal Length Lens; 2019. Url: https://www.edmundoptics.com/p/50mm-c-series-vis-nir-fixed-focal-length-lens/22385/.

[17] Optics E. 300 Grooves, 25mm Sq, 17.5 Blaze Angle Grating; 2019. Url: https://www.edmundoptics.eu/p/300-grooves-25mm-sq-175deg-blaze-angle-grating/10092/. Online.

[18] Optical K. Schott B270 Properties. Advanced Optics; 2019.

[19] Fisher M, Burt T. Rapid, Automated, Quality Control Measurements of Diffraction Grating Efficiency. Agilent Technologies. 2018;.

[20] Thorlabs. Mounted Optical Slits;. Url: https://www.thorlabs.com/thorproduct.cfm?partnumber=S50RD

[21] Technologies HO. Precision Optical Slits; 2019. Url: http://www.ealingcatalog.com/opto-mechanics/apertures/slits/precision-optical-slits.html.

[22] Sznajder M. Degradation of Materials under Space Conditions - Extrapolation of Short Term Laboratory Results on Long Term Space Mission Effects. University of Bremen; 2016.

[23] Tuan Tran, Tord Hansen Kaasa, Henrik Galtung. HSI Payload Platform Thermal Analysis Report. HYPSO Project Team; 2019. HYPSO-ANA-008.

[24] Peatross J. Physics of Light and Optics. Brigham Young University; 2019.

[25] Text CL. Electromagnetic Radiation; 2019. Accessed 4.05.2019. Online.

[26] Callister WD. Materials science and engineering. SI Version. ninth ed. Wiley; 2014.

[27] Wang B. Nature of Radiation-Induced Defects in Quartz. Chemical Physics. 2015;.

[28] Dodd SCG. High Energy Radiation Effects in Optical Elements. University of London; 2003.

[29] Martin A. An Introduction to Radiation Protection. Shaw P, editor. Chapman and Hall; 2006.

[30] Hines RL. Radiation Effects of Bombardment of Quartz and Vitreous Silica by 7.5-kev to 59-kev Positive Ions. Phys Rev. 1960;119.

[31] Adrian C Wright (auth) LSDLGe G Pacchioni. Defects in SiO2 and Related Dielectrics: Science and Technology. 1st ed. NATO Science Series 2. Springer Netherlands; 2000. Available from: http://gen.lib.rus.ec/book/index.php?md5=42719c6ba5087dc9330a6ce422102068.

[32] Kim J. Radiation damage effects in Ga2O3 materials and devices. Journal of Materials Chemistry C. 2019;7.

[33] Choppin GR. Radiochemistry and Nuclear Chemistry. 3rd ed.; 2002.

[34] Norberg C. Human Spaceflight and Exploration. Springer; 2013.

[35] Robbins M. Final Test Guideline; 2014.

[36] Hyperphysics. Particles in Cosmic Rays;. Accessed 11.04.2019. Available from: http://hyperphysics.phy-astr.gsu.edu/hbase/Astro/cosmic.html.

[37] Kossert K, Marganiec-Gałazka J, Mougeot X, Nähle OJ. Activity determination of 60Co and the importance of its beta spectrum. Applied Radiation and Isotopes. 2018;134:212–218.

[38] Drobny JG. 1 - Introduction. In: Drobny JG, editor. Ionizing Radiation and Polymers. Plastics Design Library. William Andrew Publishing; 2013. p. 1 – 10. Available from: http://www.sciencedirect.com/science/article/pii/B9781455778812000018.

[39] Astronautmegashock. How Does NASA Deal With Static Electricity Buildup?; 2019. Url:https://sites.google.com/a/lansinglions.org/astronautmegashock/how-does-nasa-deal-with-static-electricity-buildup. [Online] downloaded 9th may 2019.

[40] Lint VAJ. Mechanisms of Radiation Effects in Electronic Materials. John Wiley & Sons; 1980.

[41] Poivey C. TNID Total Non Ionizing Dose or DD displacement damage. ESA; 2017. .

[42] Lyndon B. Understanding Space Radiation; 2002. NASA Facts.

[43] Grieder PKF. Cosmic Rays at Earth. ELSEVIER; 2001.

[44] Mikaelian T. Spacecraft Charging and Hazards to Electronics in Space. Physics of the Space Environment. 2001;.

[45] Heirtzler J. The future of the South Atlantic anomaly and implications for radiation damage in space. Journal of Atmospheric and Solar-Terrestrial Physics. 2002;64(16):1701–1708.

[46] Newell HE, Naugle JE. Radiation Environment in Space. Science. 1960;132(3438):1465–1472. Available from: http://www.jstor.org/stable/1707147.

[47] Gupta V. Analysis of single event radiation effects and fault mechanisms in SRAM, FRAM and NAND Flash. Application to the MTCube nanosatellite project. University of Montepellier; 2017.

[48] Anwar B, Acton L, Hudson H, Makita M, McClymont A, Tsuneta S. Rapid sunspot motion during a major solar flare. Solar physics. 1993;147(2):287–303.

[49] Index SS, term Solar Observations L. Monthly and smoothed sunspot number; 2019. Accessed 08.04.2019. Available from: `http://www.sidc.be/silso/monthlyssnplot`.

[50] Lummerzheim D. Modeling and Forecasting Aurora. Computing in Science & Engineering. 2007 10;9:53–61.

[51] Space engineering: Space environment;.

[52] Carreau C. Earth's Plasmasphere and the Van Allen Belts; 2013. Accessed 20.03.2019. Available from: `http://sci.esa.int/cluster/52831-earth-plasmasphere-and-the-van-allen-belts/`.

[53] Code C. Human Radiation Van Effects Allen Belts; 2019. Url:https://cellcode.us/quotes/human-radiation-van-effects-allen-belts.html Accsess June 2019. Online.

[54] Space Product Assurance Determination of the susceptibility of metals to stress-corrosion cracking;.

[55] Norbury JW. Opinion/Position Paper Galactic cosmic ray simulation at the NASA space radiation laboratory. Life Sciences in Space Research. 2008;.

[56] OMERE. OMERE user manual;. OMERE 5.2.5.0.

[57] TRAD. OMERE; 2019. URL: http://www.trad.fr/en/space/omere-software/ Accessed 3rd may 2019. Online.

[58] MIT. Mesh convergence;. Accessed 4th April 2019. Online.

[59] Inc AG, editor. STK Products. AGI; 2019. Url: https://www.agi.com/products.

[60] Global Plastic Sheeting. Mil Thickness Of Plastic Sheeting in millimeters and inches; 2019. Url: https://www.globalplasticsheeting.com/mil-thickness-compared-to-mm-millimeter-and-inches. online.

[61] Was GS. Fundamentals of radiation materials science: metals and alloys. Springer; 2016.

[62] Reichmanis E. Irradiation of Polymeric Materials. American Chemical Society; 1993.

[63] Anwar A. Outgassing Effect on Spacecraft Structure Materials. International Journal of Astronomy, Astrophysics and Space Science. 2015;p. 34–38.

[64] Wassman W. The Materials Used in Artificial Satellites and Space Structures. AZO Materials. 2015;.

[65] Zinkle S. Radiation-induced changes in the physical properties of ceramic materials. Journal of Nuclear Materials. 1992;.

[66] Zinkle S. Radiation effects in ceramics. Journal of Nuclear Materials. 1994;.

[67] Walrafen GE, Revesz AG. Structure and bonding in noncrystalline solids. Springer Science & Business Media; 2012.

[68] Skuja L, Hosono H, Hirano M. Laser-induced color centers in silica. In: Laser-Induced Damage in Optical Materials: 2000. vol. 4347. International Society for Optics and Photonics; 2001. p. 155–169.

[69] Chiu PK, Chiang D, Lee CT, Lin YW, Hsiao CN. Optical properties and crystallinity of silver mirrors under a 35 krad cobalt-60 radiation. Journal of Vacuum Science & Technology A: Vacuum, Surfaces, and Films. 2015;33(5):05E104.

[70] Devine R. Radiation damage and the role of structure in amorphous SiO2. Nuclear Instruments and Methods in Physics Research Section B: Beam Interactions with Materials and Atoms. 1990;46(1-4):244–251.

[71] Sun C. Formation of E Centers Under Electron Irradiation in Ultrapure Glass and Structural Relaxation. Protection of Materials and Structures from the Space Environment. 2011;.

[72] Bergstrm J. 2 - Experimental Characterization Techniques. In: Bergstrm J, editor. Mechanics of Solid Polymers. William Andrew Publishing; 2015. p. 19 – 114. Available from: http://www.sciencedirect.com/science/article/pii/B9780323311502000029.

Appendix

5.7 Risk Report

Risk Manager sluttrapport

	Konsekvensområde	Resultat	Resultat etter tiltak
▲ *Farekilde:* Lab i Danmark [55466]			
▲ *Uønsket hendelse:* Gamma stråling fra Cobolt 60 [68969]			
	Helse	Akseptabel risiko	
▲ *Uønsket hendelse:* Innhalere ozon [0]			
	Helse	Akseptabel risiko	

Endelige vurderinger (må fylles ut før lukking) *

Fyll ut begrunnelser og kommentarer til restrisiko, samt om usikkerhet ved vurderingen (f.eks. om den er av generell art, om vurderingen er basert på få personer etc.).

Laboratorier for radioaktiv stråling er i utgangspunktet svært helsefarlige, men er på grunn av dette konstruert for å beherske dette med tykke bly vegger. I følge personlettet ved labben på DTU er strålingsdosene lavere enn en flytur fra Norge til Danmark. Ionisering av oksygen kan også produsere ozon, en skal derfor ikke oppholde seg mer enn nødvendig nær prøvekammeret.

5.8 Component Lifetime Radiation Test

Component Lifetime Radiation Test

General information

Test type:

- Static

Validation method:

- Characterization test: Dark current and radiometric test
- Visual Inspection of glass opacity

Purpose

The main purpose of this test is to explore radiation degradation of components of the HSI. Exposure to the levels of radiation present in LEO is expected to darken the glass of the 50mm VIS-NIR lens as well as the grating itself. The performance after radiation exposure of the imager is unknown, this will therefore be an exploratory test into the performance of key components after increasingly higher doses of radiation, simulating an approximated lifetime in LEO.

Risk assessment

Testing with a high radiation dose should only be conducted in a shielded environment due to hazard of radiation. As per the standard HYPSO test procedure, all HSE rules and procedures for the relevant lab shall be adhered to.

Radiation testing is destructive and will damage the tested components. Expected damage comprises of darkening of lenses and grating, imager malfunction, memory corruption. Tested components must be clearly marked.

Items to be tested

Table 1: Test item list

Test Items	No. of items	Approximate dimensions [mm]	Test Description	Test date
50 mm VIS-NIR lens	1	35.8x35.8x53.7	Lens to be exposed to radiation.	26.03.2019
Sony IMX249 (UI-5260CP-M-GL R2) sensor	1	29x29x48	Imager module to be exposed to radiation.	26.03.2019
Grating	1	25 x 25 x 3	Grating to be exposed to radiation.	26.03.2019
Precision Slit	1	20 x 20	Precision slit to be exposed to radiation.	26.03.2019
Sensor protective lens	1		Lens to be exposed to radiation.	26.03.2019

Test approach

Establish a baseline performance of the components, using the standard characterization: Radiometric approach. (The baseline are established by characterization tests that are developed to quantize the amount of darkening taking place.)

Two sets of imagers and lenses are required for the test, one set of test items and one set for control and and to provide cross-checking between components. To acquire accurate data of the rate of darkening and other degradation it is paramount that the radiation dosing happens in increments that would at most equal a years worth of radiation per dose. Table 2 shows the radiation intervals. One grating and one precision slit will also be tested.

Characterization tests are developed to quantize the degradation of the components and these will be performed after every radiation dose, thus requiring removal and reinsertion of test objects in the radiation chamber. These test will consist of:

- Dark current test (sensor)
- Radiometric test (sensor, lens)
- Visual inspection (sensor, lens, grating, precision slit)

Radiation amount

Calculation of radiation, effects and margin: ECSS-Q-HB-10-12A
SPENVIS Simulation software
The radiation dose simulating a lifetime of 5 years in LEO is estimated by:

Table 2: Radiation intervals (Specific values might change)

Dosage No. #	Radiation Rate [Gy/min]	Elapsed "real time" [years]	Total elapsed lifetime [years]	Radiation dose [Gy] +/-20%	Total Dose [Gy] +/-20%
1	5	0.5	0.5	10	10
2	5	0.5	1	10	20
3	5	1	2	20	40
4	5	1	3	60	100

Estimated time (with 30 min for characterization between tests): 8.5 hours

Scale of parts to be tested

Figure 1 shows the scale of the test items.

Figure 1: Item Scale

5.9 Convergence study

5.9.1 Convergence study points per orbit

The simulating perform overlapping results when more that 50 points per orbits are used.

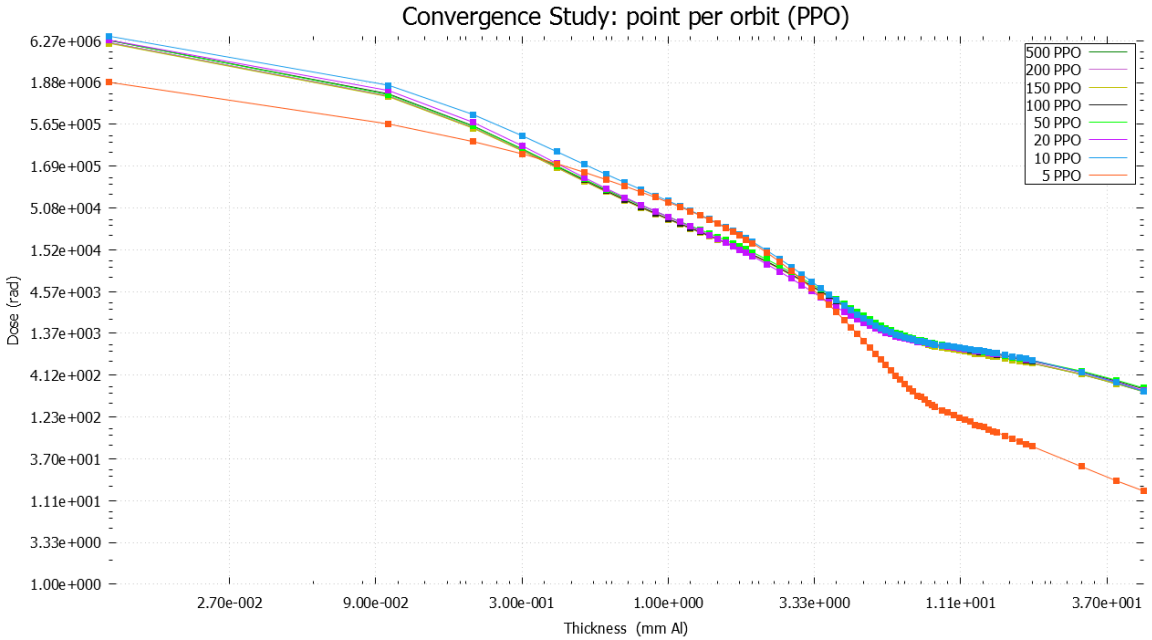
Convergence Study: point per orbit (PPO)
Dose (rad)
6.27e+006
1.88e+006
5.65e+005
1.69e+005
5.08e+004
1.52e+004
4.57e+003
1.37e+003
4.12e+002
1.23e+002
3.70e+001
1.11e+001
3.33e+000
1.00e+000
2.70e-002
9.00e-002
3.00e-001
1.00e+000
3.33e+000
1.11e+001
3.70e+001
Thickness (mm Al)
500 PPO
200 PPO
150 PPO
100 PPO
50 PPO
20 PPO
10 PPO
5 PPO

5.9.2 Convergence study number of orbits

The simulating perform overlapping results when more that 15 orbits are used.

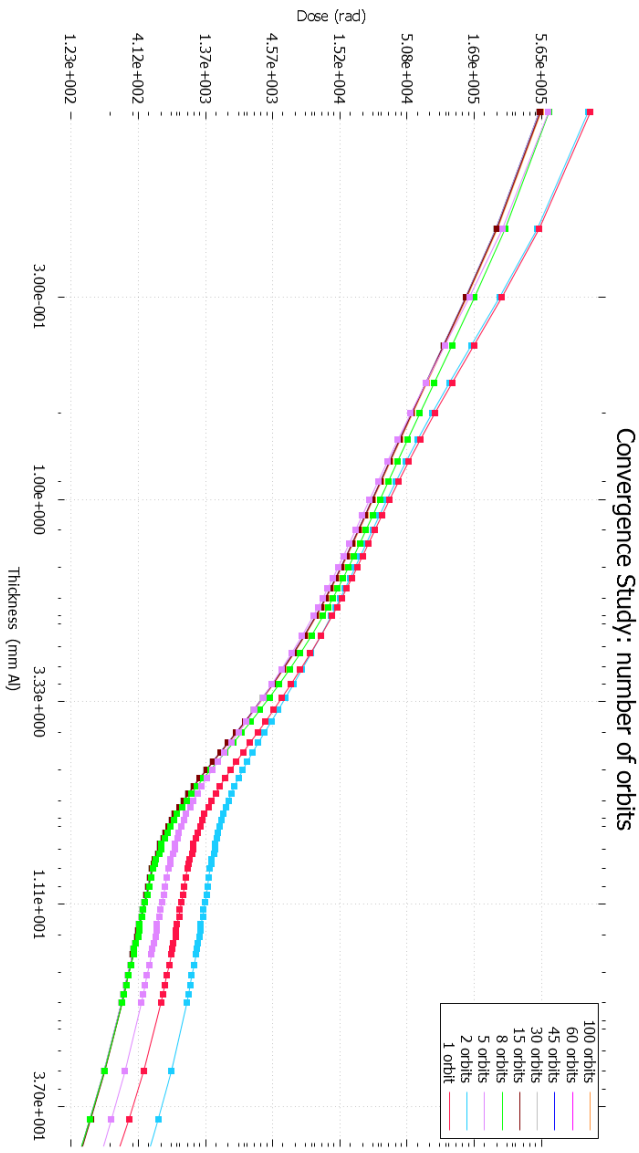
Convergence Study: number of orbits
Dose (rad)
5.65e+005
1.69e+005
5.08e+004
1.52e+004
4.57e+003
1.37e+003
4.12e+002
1.23e+002
Thickness (mm Al)
3.00e-001
1.00e+000
3.33e+000
1.11e+001
3.70e+001
100 orbits
60 orbits
45 orbits
30 orbits
15 orbits
8 orbits
5 orbits
2 orbits
1 orbit

5.10 EDS results

The following 6 Appendix items are the EDS spot analysis

5.10.1 1st lens EDS

A point EDS of surface of the 1st optical lenses of the objective

View016

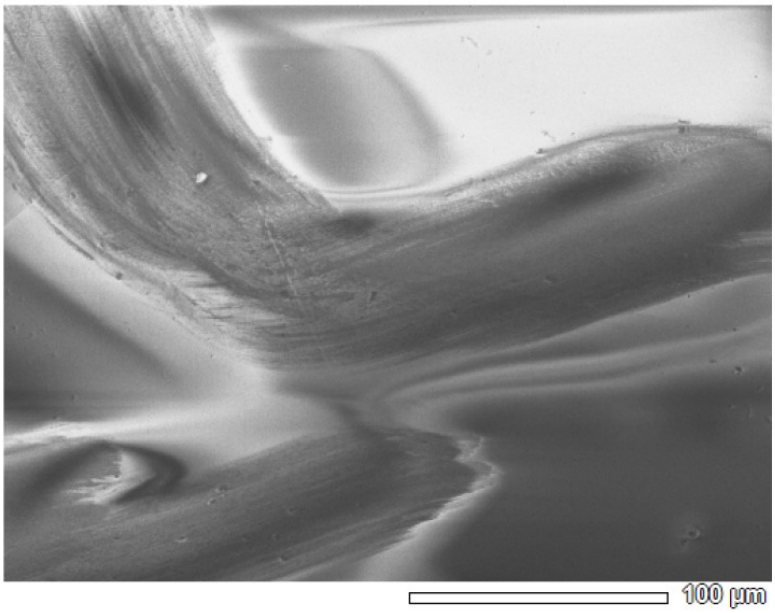

Title	: BF
Instrument	: JCM-6000
Volt	: 15.00 kV
Mag.	: x 400
Date	: 2019/05/08
Pixel	: 512 x 384

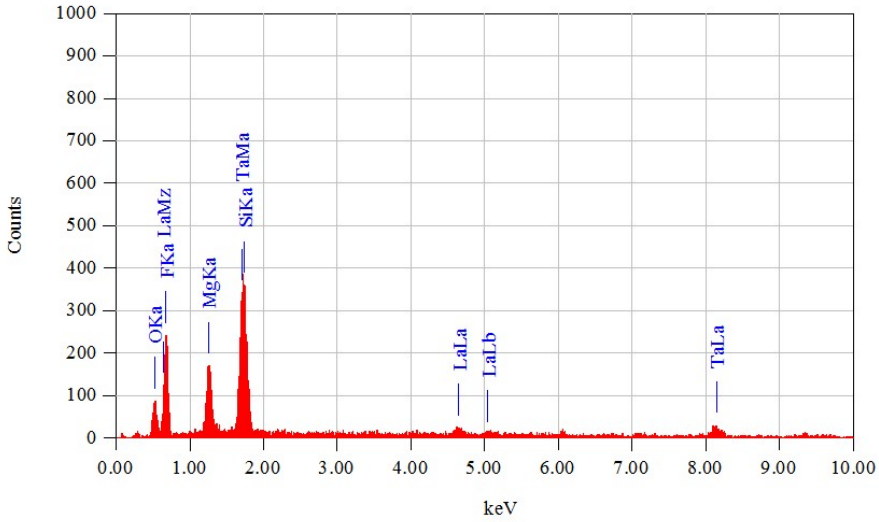

Acquisition Parameter

Instrument	: JCM-6000
Acc. Voltage	: 15.0 kV
Probe Current	: 1.00000 nA
PHA mode	: T3
Real Time	: 285.58 sec
Live Time	: 285.15 sec
Dead Time	: 0 %
Counting Rate	: 87 cps
Energy Range	: 0 - 20 keV

ZAF Method Standardless Quantitative Analysis
Fitting Coefficient : 0.1639

Element	(keV)	Mass%	Sigma	Atom%	Compound	Mass%	Cation	K
Si K	1.739	3.26	0.39	3.55				3.3143
La L*	4.648	4.30	0.33	0.95				6.5395
Mg K	1.253	8.79	0.27	11.05				6.3724
O K	0.525	13.84	0.44	26.42				11.7650
F K	0.677	32.13	0.65	51.67				40.4191
Ta M*	1.709	37.67	1.33	6.36				31.5897
Total		100.00		100.00				

5.10.2 2nd lens EDS

A point EDS of surface of the 2nd optical lenses of the objective

View007

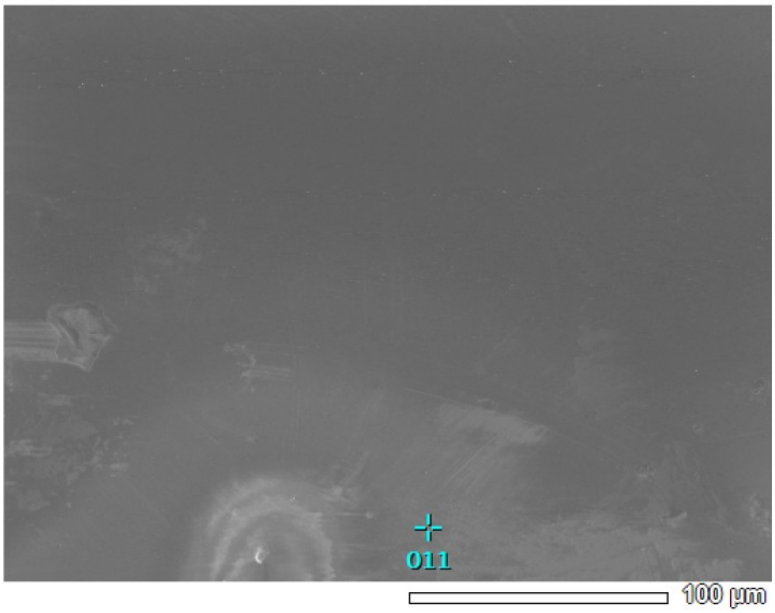

Title : BF

Instrument	: JCM-6000
Volt	: 15.00 kV
Mag.	: x 400
Date	: 2019/05/08
Pixel	: 512 x 384

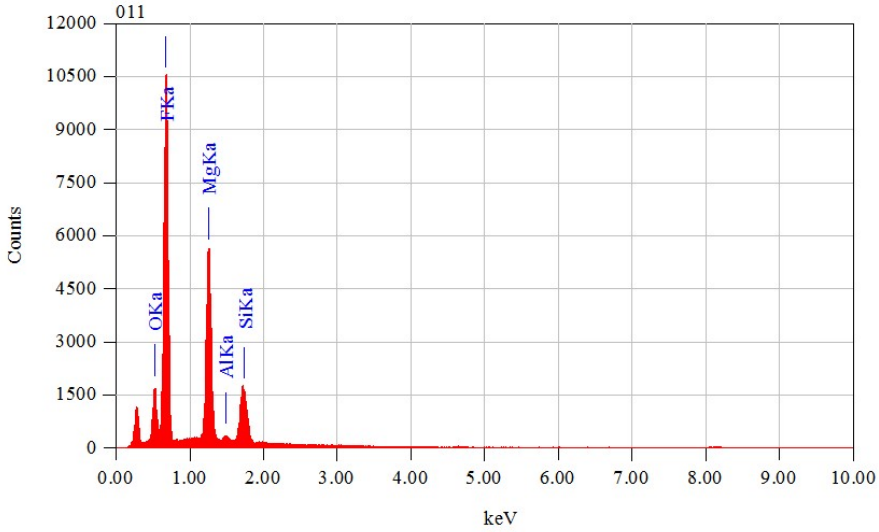

Acquisition Parameter

Instrument	: JCM-6000
Acc. Voltage	: 15.0 kV
Probe Current	: 1.00000 nA
PHA mode	: T3
Real Time	: 113.85 sec
Live Time	: 112.03 sec
Dead Time	: 1 %
Counting Rate	: 1950 cps
Energy Range	: 0 - 20 keV

ZAF Method Standardless Quantitative Analysis
Fitting Coefficient : 0.0780

Element	(keV)	Mass%	Sigma	Atom%	Compound	Mass%	Cation	K
Al K*	1.486	0.87	0.04	0.64				0.3146
Si K	1.739	4.62	0.06	3.29				2.3585
O K	0.525	10.17	0.08	12.72				9.1076
Mg K	1.253	23.68	0.12	19.48				9.3511
F K	0.677	60.65	0.18	63.86				78.8682
Total		100.00		100.00				

5.10.3 3rd lens EDS

A point EDS of surface of the 3rd optical lenses of the objective

View002

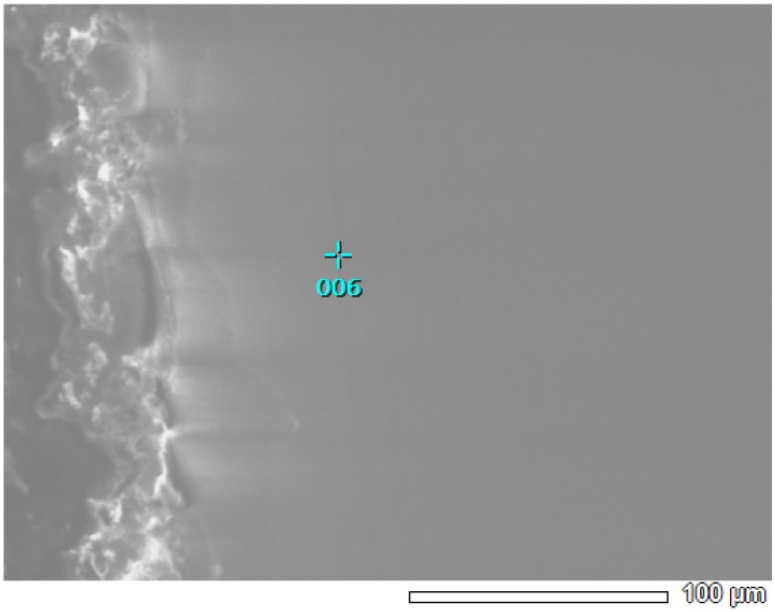


```
Title        : BF
---------------------------
Instrument   : JCM-6000
Volt         : 15.00 kV
Mag.         : x 400
Date         : 2019/05/08
Pixel        : 512 x 384
```

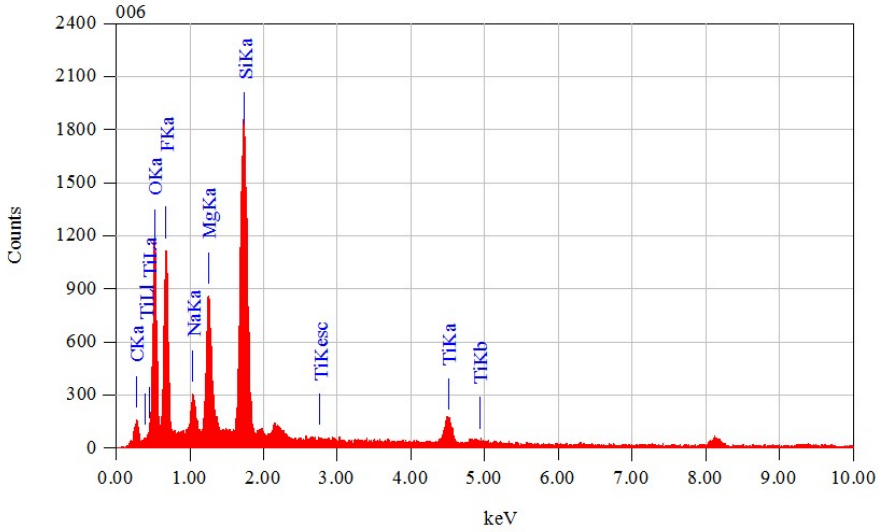


```
Acquisition Parameter
Instrument    : JCM-6000
Acc. Voltage  : 15.0 kV
Probe Current: 1.00000 nA
PHA mode      : T3
Real Time     : 150.93 sec
Live Time     : 150.00 sec
Dead Time     : 0 %
Counting Rate: 586 cps
Energy Range :  0 - 20 keV
```

ZAF Method Standardless Quantitative Analysis
Fitting Coefficient : 0.1094

Element	(keV)	Mass%	Sigma	Atom%	Compound	Mass%	Cation	K
Ti K	4.508	2.23	0.06	0.85				4.5048
Na K	1.041	2.75	0.09	2.17				1.8670
Mg K	1.253	7.46	0.12	5.57				5.7395
C K	0.277	10.61	0.16	16.03				1.8550
Si K	1.739	10.97	0.12	7.09				13.8309
O K	0.525	29.71	0.26	33.68				33.8704
F K	0.677	36.26	0.36	34.62				38.3324
Total		100.00		100.00				

5.10.4 4th lens EDS

A point EDS of surface of the 4th optical lenses of the objective

View008


```
Title        : BF
---------------------------
Instrument   : JCM-6000
Volt         : 15.00 kV
Mag.         : x 400
Date         : 2019/05/08
Pixel        : 512 x 384
```

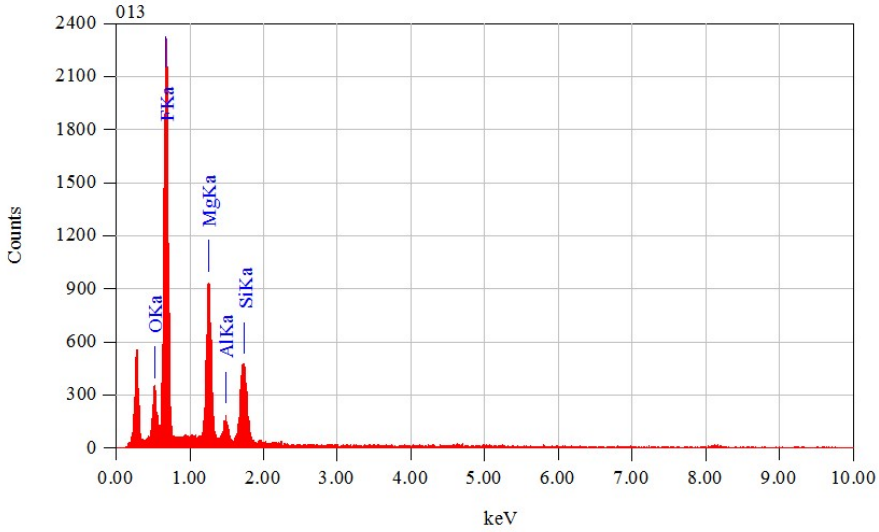


```
Acquisition Parameter
Instrument    : JCM-6000
Acc. Voltage  : 15.0 kV
Probe Current: 1.00000 nA
PHA mode      : T3
Real Time     : 57.17 sec
Live Time     : 56.73 sec
Dead Time     : 0 %
Counting Rate: 939 cps
Energy Range  :  0 - 20 keV
```

ZAF Method Standardless Quantitative Analysis
Fitting Coefficient : 0.1612

Element	(keV)	Mass%	Sigma	Atom%	Compound	Mass%	Cation	K
Al K	1.486	2.73	0.11	2.03				1.0092
Si K*	1.739	6.27	0.15	4.47				3.1386
O K	0.525	9.32	0.18	11.67				7.9079
Mg K*	1.253	18.39	0.24	15.15				6.7819
F K	0.677	63.29	0.41	66.69				81.1624
Total		100.00		100.00				

5.10.5 5th lens EDS

A point EDS of surface of the 5th optical lenses of the objective

View010

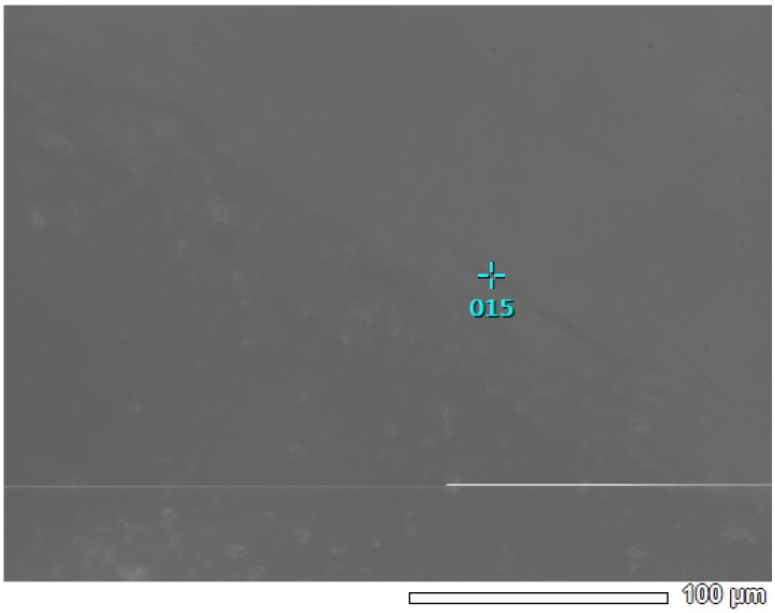

Title	: BF
Instrument	: JCM-6000
Volt	: 15.00 kV
Mag.	: x 400
Date	: 2019/05/08
Pixel	: 512 x 384

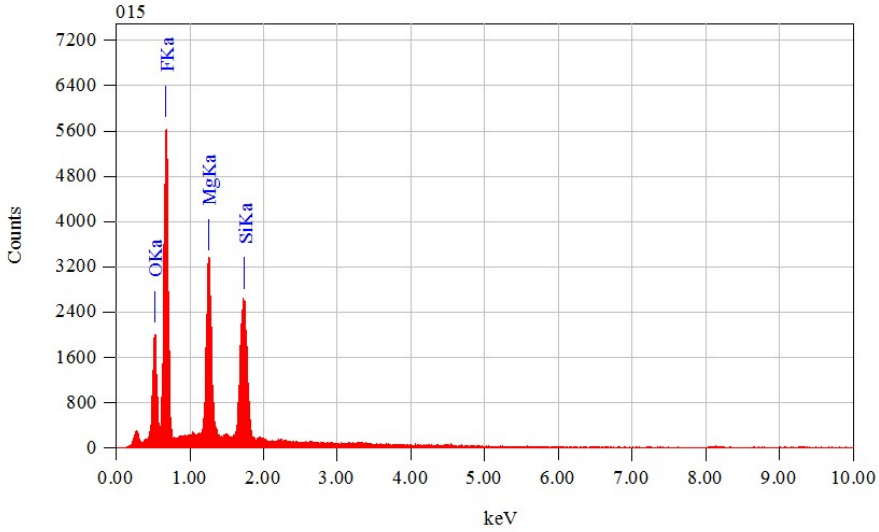

Acquisition Parameter	
Instrument	: JCM-6000
Acc. Voltage	: 15.0 kV
Probe Current	: 1.00000 nA
PHA mode	: T3
Real Time	: 65.90 sec
Live Time	: 64.38 sec
Dead Time	: 2 %
Counting Rate	: 2725 cps
Energy Range	: 0 - 20 keV

ZAF Method Standardless Quantitative Analysis
Fitting Coefficient : 0.0608

Element	(keV)	Mass%	Sigma	Atom%	Compound	Mass%	Cation	K
Si K	1.739	9.14	0.07	6.41				6.1592
O K	0.525	17.13	0.07	21.10				18.4826
Mg K	1.253	17.62	0.09	14.29				8.3480
F K	0.677	56.10	0.14	58.20				67.0102
Total		100.00		100.00				

5.10.6 6th lens EDS

A point EDS of surface of the 6th optical lenses of the objective

View022

Title : BF

Instrument	: JCM-6000
Volt	: 15.00 kV
Mag.	: x 400
Date	: 2019/05/08
Pixel	: 512 x 384

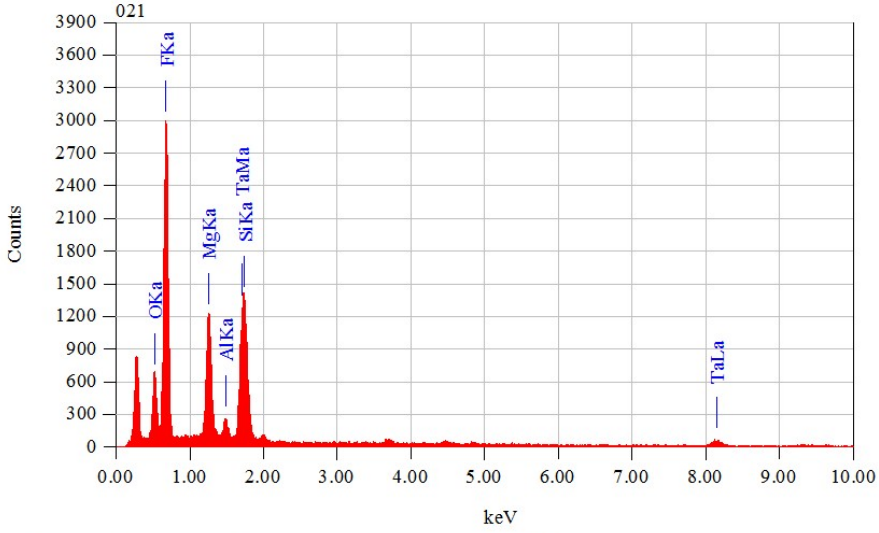

Acquisition Parameter

Instrument	: JCM-6000
Acc. Voltage	: 15.0 kV
Probe Current	: 1.00000 nA
PHA mode	: T3
Real Time	: 75.51 sec
Live Time	: 74.67 sec
Dead Time	: 1 %
Counting Rate	: 1377 cps
Energy Range	: 0 - 20 keV

ZAF Method Standardless Quantitative Analysis
Fitting Coefficient : 0.1519

Element	(keV)	Mass%	Sigma	Atom%	Compound	Mass%	Cation	K
Al K	1.486	1.31	0.05	1.15				0.8166
Si K*	1.739	3.14	0.13	2.64				2.5022
Mg K	1.253	10.63	0.12	10.35				5.8584
O K	0.525	12.23	0.15	18.09				10.9428
Ta M	1.709	20.47	0.45	2.68				12.9752
F K	0.677	52.22	0.30	65.08				66.9049
Total		100.00		100.00				

5.10.7 XRD results

XRD results.

1st lens, facing the light view.

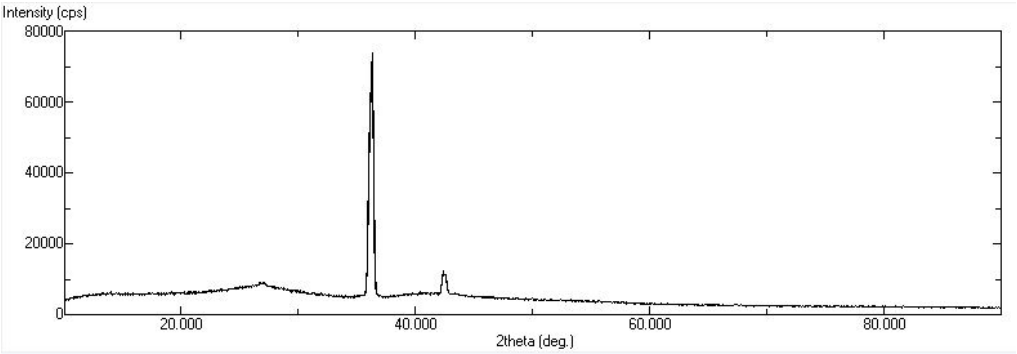

1st lens, facing the sensor view.

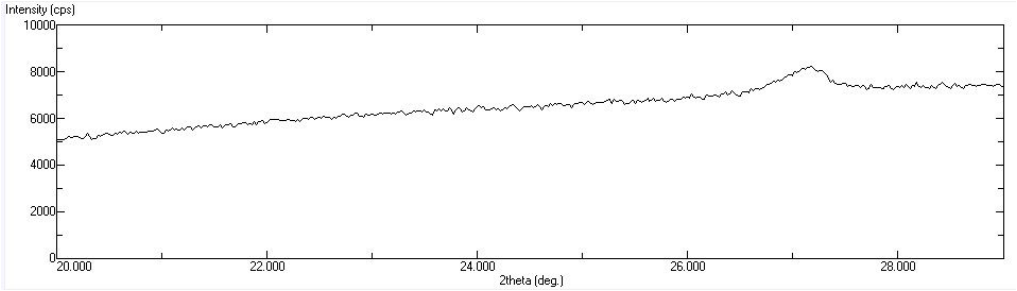

6th lens, facing the light view.

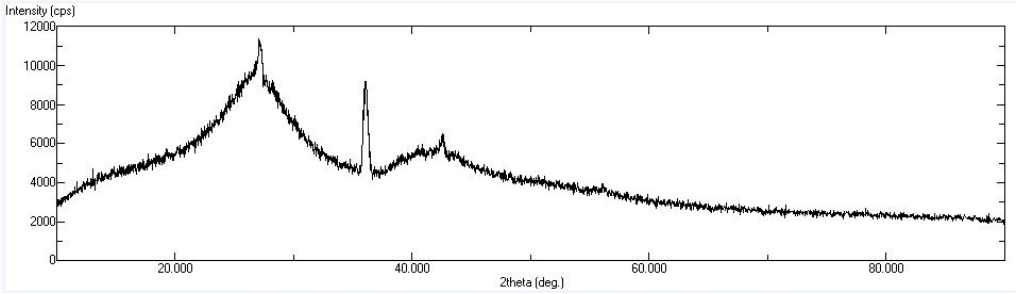

6th lens, facing the sensor view.